Section 1

Atmospheric data assimilation schemes, analysis and initialization, data impact studies, observing system experiments

The Impact of Ground-Based Microwave Radiometer Data to Estimation of Thermodynamic Profiles in Low-Level Troposphere

Kentaro Araki, Masataka Murakami, Hiroshi Ishimoto, and Takuya Tajiri

Meteorological Research Institute, Tsukuba, Japan
e-mail: araki@mri-jma.go.jp

1. Introduction

In order to forecast and nowcast severe storms, temporally and spatially high-resolution estimation of thermodynamic and dynamic environments is highly required. A ground-based microwave radiometer profiler (MWR) has been used to retrieve vertical profiles of atmospheric temperature, water vapor, and liquid water content at time intervals within a few minutes. As retrieval methods, various inversion methods such as neural networks (NNs) and variational techniques (e.g., Araki et al. 2014; Ishimoto 2015) have been proposed. Recently, variational approaches have been known to outperform other methods in retrieving vertical profiles of atmospheric temperature and water vapor, especially in lower troposphere. These approaches are based on the data assimilation of 1-dimensional variational (1DVAR) techniques which combine radiometric observations with the outputs from numerical weather prediction model. The purpose of this study is to investigate the effectiveness of a new 1DVAR method using zenith and off-zenith observations. Using the MWR observation data collected at Tsukuba, Japan, NN- and 1DVAR-derived thermodynamic profiles are compared with radiosonde observations.

2. Accuracy of 1DVAR-derived thermodynamic profiles

In this study, we used the ground-based multi-channel MWR (model: MP-3000A, Radiometrics) installed at the Meteorological Research Institute of Japan Meteorological Agency (JMA) in Tateno, at 36.05°N, 140.13°E. The MWR observes the brightness temperatures (TBs) of 21 K-band (22–30 GHz) and 14 V-band (51–59 GHz) microwave channels with the band width of 300 MHz in zenith direction and at an elevation angle of 15° in north and south azimuth directions, the radiation temperature of one zenith-looking infrared (9.6–11.5 μm wavelength) channel, and the in situ surface atmospheric temperature, relative humidity, and pressure. A rain sensor is also combined with the MWR. The MWR observations were sccessfully conducted from 25 April to 27 June 2012, and the radiosonde observations at the JMA station in Tateno during this period were used for verification of retrieved vertical profiles of temperature and water vapor density. The vertical resolutions of NN-derived profiles are 50 m from the surface to 500 m, 100 m to 2 km, and 250 m to 10 km.

The 1DVAR technique used in this study is based on Ishimoto (2015). In this method, retrieval variables $\mathbf{x}$ represents profiles of atmospheric temperature and water vapor density. The iterative solution that minimizes the cost function is given by

$$\mathbf{x_{i+1}} = \mathbf{x_i} + (\mathbf{B}^{-1} + \mathbf{H_i}^T\mathbf{R}^{-1}\mathbf{H_i})^{-1}[\mathbf{H_i}^T\mathbf{R}^{-1}(\mathbf{y} - \mathbf{F}(\mathbf{x_i})) - \mathbf{B}^{-1}(\mathbf{x_i} - \mathbf{x_b})]$$

where $\mathbf{x_i}$ and $\mathbf{x_b}$ are current and background state vectors, respectively; $\mathbf{H_i}$ is the Jacobian matrix of the observation vector with respect to the state vector; $\mathbf{B}$ and $\mathbf{R}$ are the error-covariance matrices of $\mathbf{x_b}$ and of the observation vector $\mathbf{y}$, respectively; and $\mathbf{F}(\mathbf{x_i})$ is the forward model operator. Note that the zenith and off-zenith observations are separately used as the observation vectors in this study. By using the off-zenith observations as the observational vectors, the sensitivities to water vapor and atmospheric temperature increase in all altitudes and in low-level troposphere, respectively (not shown).

The numerical model used in this study is the JMA non-hydrostatic model (NHM; Saito et al. 2006). Numerical experiments with a horizontal grid spacing of 5 km and a domain covering Japan were performed. The 24-hour atmospheric conditions were simulated from 24 hours before each radiosonde observation. The initial and boundary conditions were provided from 3-hourly JMA mesoscale analyses and the 1-hourly forecasts of the JMA operational global spectrum model, respectively. The time step of the simulation was 20 seconds, and the results were output at 10-minute intervals. Other setups were the same as those used in Saito et al. (2006). Vertical profiles averaged over 25 × 25 km squares centered at Tateno were interpolated to MWR observation times and used for the 1DVAR retrievals. The vertical profiles derived from Sonde, NHM, and 1DVAR were interpolated according to the NN altitude resolution. In this study, NN-, NHM-, and 1DVAR-derived profiles averaged for 30 minutes before each radiosonde observation were compared with Sonde-derived profiles.

Figure 1 shows the vertical profiles of mean difference (MD), standard deviation (STD) and root-mean-square (RMS) error of NN-, 1DVAR-, and NHM-derived atmospheric temperature with respect to Sonde-derived profiles for cases where a rain sensor didn't observe rain 1 hour before and after the radiosonde observations between 25 April and 27 June 2012 (87 cases). The inferiors of Z, S, and N in NN and 1DVAR respectively indicate the retrievals using zenith, off-zenith observations in southern and northern azimuth directions. Figure 2 is same as Fig. 1 but for water vapor density.

NHM- and 1DVAR-derived temperature profiles showed good agreement; the absolute MD was less than 1 K

in any altitudes (Fig. 1). The STD and RMS error for 1DVAR-derived temperature were about 1 K in any altitudes, but those of NHM-derived one reached 1.5 K below 0.5 km. The absolute MD for NHM- and 1DVAR-derived water vapor densities was less than 0.5 g m^{-3} in any altitudes, and the values of 1DVAR-derived one were less than that of NHM-derived one (Fig. 2). The STD and RMS error for 1DVAR-derived vapor density were less than 1.5 g m^{-3} in any altitudes, although those of NHM-derived one reached 2 g m^{-3} at around 1 km. The result shows 1DVAR technique successfully improves the thermodynamic profiles especially in low troposphere as compared to the other methods. Cimini et al. (2011) investigated the accuracy of vertical profiles obtained by a different 1DVAR technique using off-zenith observations as observational vectors and the 1-hourly analyses provided by the NOAA Local Analysis and Prediction System as the first guesses, and showed that their 1DVAR technique outperformed the analyses. Although their study used the MWR observation data during a winter season when there was less water vapor, our results showed that the 1DVAR technique also significantly improved the accuracy of water vapor profiles in comparison with NHM simulation results even in a warm season when water vapor concentrations are much higher than winter season.

3. Conclusions and remarks

A new 1DVAR technique using MWR observations was applied and the accuracy of retrieved thermodynamic profiles was statistically investigated. The comparisons with radiosonde observations showed that the 1DVAR technique successfully improved the vertical profiles of temperature and water vapor density, especially in low troposphere as compared to retrievals by neural networks and numerical simulation results. This result suggests that the 1DVAR technique is helpful in nowcasting the severe storms. It's also desired that the impact of MWR data used in cloud-resolving four-dimensional variational data assimilation system on the accuracy of severe storm forecast will be investigated.
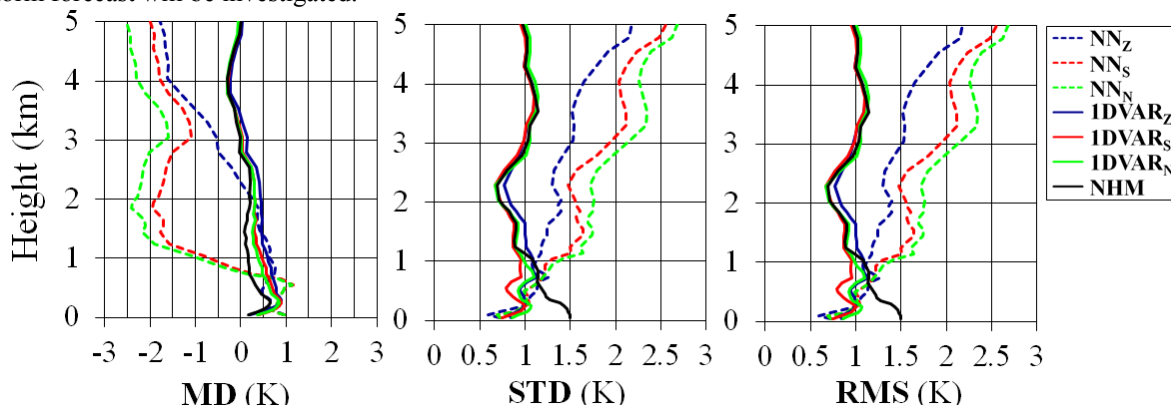

Figure 1. Mean difference (MD), standard deviation (STD) and root-mean-square (RMS) error of NN-, 1DVAR-, and NHM-derived atmospheric temperature with respect to radiosonde soundings.
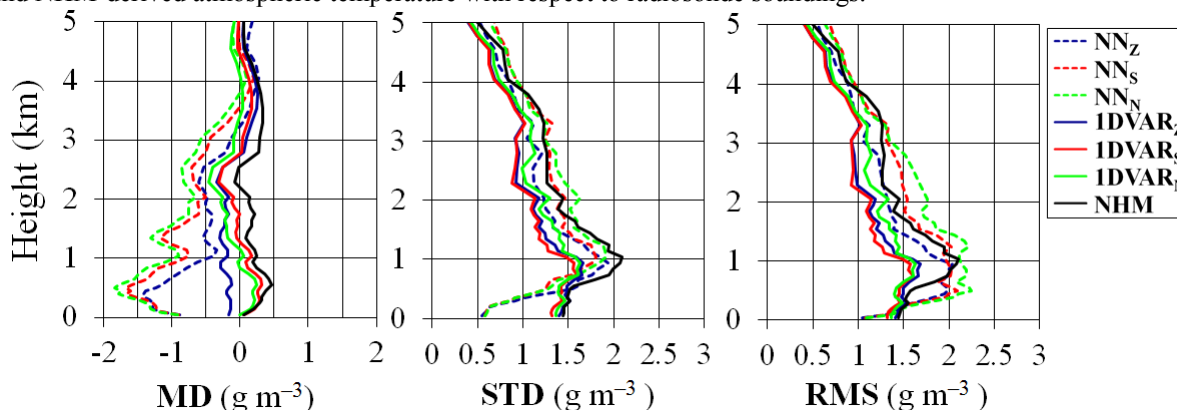

Figure 2. Same as Fig. 1, but for water vapor density.

References:
Araki, K., H. Ishimoto, M. Murakami, and T. Tajiri, 2014: Temporal variation of close-proximity soundings within a tornadic supercell environment. *SOLA*, **10**, 57–61.
Cimini, D., E. Campos, R. Ware, S. Albers, G. Giuliani, J. Oreamuno, P. Joe, S. E. Koch, S. Cober, and E. Westwater, 2011: Thermodynamic atmospheric profiling during the 2010 winter Olympics using ground-based microwave radiometry. *IEEE Trans. Geosci. Remote Sens.*, **49**, 4959–4969.
Ishimoto, H., 2015: Analysis of microwave radiometric data using a 1DVAR technique. *Meteor. Res. Notes*, (in press, in Japanese).
Saito, K., T. Fujita, Y. Yamada, J. Ishida, Y. Kumagai, K. Aranami, S. Ohmori, R. Nagasawa, S. Kumagai, C. Muroi, T. Kato, H. Eito, and Y. Yamazaki, 2006: The operational JMA nonhydrostatic mesoscale model. *Mon. Wea. Rev.*, **134**, 1266–1298.

Application of 1DVAR Technique using Ground-Based Microwave Radiometer Data to Estimation of Temporally High-Resolution Thermodynamic Environments in a Tornadic Supercell Event

Kentaro Araki, Masataka Murakami, Hiroshi Ishimoto, and Takuya Tajiri

Meteorological Research Institute, Tsukuba, Japan
e-mail: araki@mri-jma.go.jp

1. Introduction

The prediction and nowcast of significant tornadic (SIGTOR) supercells remain challenging because the environments favorable for supercells are not well understood. Although several previous studies have examined proximity soundings within supercell environments, no study has provided information on temporal variations of SIGTOR supercell environments at intervals of a few minutes.

Recently, ground-based microwave radiometer profilers (MWRs) have been used to retrieve vertical profiles of air temperature and water vapor density at time intervals of a few minutes. Araki et al. (2015) showed that 1-dimensional variational (1DVAR, Ishimoto 2015) technique, which combines radiometric observations with outputs from a numerical weather forecast model reduced the error in thermodynamic profiles derived from numerical simulations, especially in low-level troposphere.

The purpose of this study is to investigate the temporal variation, at intervals of a few minutes, of the environment of a supercell which caused a significant tornado (rank F3) in the northern part of the Tsukuba city in Japan on 6 May 2012. MWR observations were successfully conducted at the Meteorological Research Institute (MRI) in Tsukuba at distances less than 20 km from the tornado. We used a 1DVAR technique (Araki et al. 2015) to obtain the thermodynamic profiles and examined the temporal variations of several supercell and tornado forecast parameters by using both 1DVAR-derived thermodynamic profiles and wind profiles obtained from numerical simulations. The details of this study are described in Araki et al. (2014).

2. Temporal variation of tornado forecast parameters

We used the ground-based MWR (MP-3000A, Radiometrics) installed at the MRI in Tateno (in Tsukuba), at 36.05°N, 140.13°E. The MWR observes the brightness temperatures of 21 K-band (22–30 GHz) and 14 V-band (51-59 GHz) microwave channels at zenith direction. The details and accuracy of the 1DVAR technique used in this study are given by Ishimoto (2015) and Araki et al. (2015), respectively. We performed a numerical experiment using the JMA non-hydrostatic model (NHM; Saito et al. 2006) with a horizontal grid spacing of 1 km and a model domain covering the Kanto Plain, and the result was used for the first guess in the 1DVAR analysis.

The Tsukuba F3 tornado occurred 13–17 km northwest of Tateno from 1235 to 1251 JST on 6 May 2012 (Fig. 1). A classic supercell with a well-defined hook echo moved east-northeastward along the low-level convergence line formed by warm southwesterly and cold northwesterly flows to the northwest of Tateno. The surface networks observed warm southerly flows and no rainfall at Tateno during the event. These conditions were suitable for the MWR at Tateno to observe the supercell environment.

Time-height cross sections of water vapor density derived from 1DVAR and NHM, and the difference of them between 0900 and 1500 JST are shown in Fig. 2. In the NHM-derived
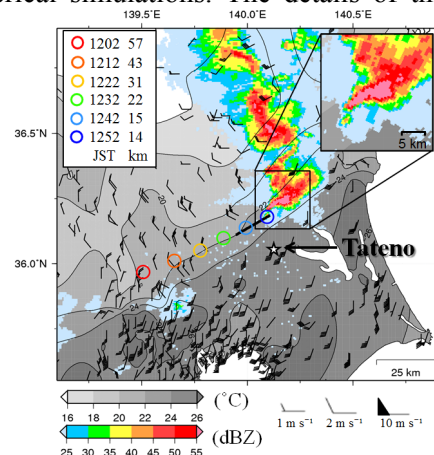

Figure 1. Observed features of the tornadic supercell on 6 May 2012. Surface air temperature (gray), wind (barbs) at 1300 JST, provided by surface networks. PPI reflectivity observed by the Tokyo Doppler radar at an elevation angle of 1.7° at 1252 JST. The white star and the black solid line indicate the location of Tateno and the path of the tornado, respectively. Colored circles indicate the locations of the hook echo observed on the PPIs at the same elevation angle; the observation times and the distances from Tateno are shown in the upper-left corner.

profiles, the thickness of the layer with water vapor density greater than 12 g m^{-3} was about 1 km. From the result of Araki et al. (2015), NHM-derived water vapor density between 500 m and 1 km has a positive bias and error of about 2 g m^{-3}. The 1DVAR-derived profiles successfully reduced the high water vapor density between 500 m and 1 km by more than 1.5 g m^{-3}.

Time series of mean layer (0–1 km) convective available potential energy (MLCAPE), storm relative helicities of 0–1 and 0–3 km (SRH1km, SRH3km), and significant tornado parameter (STP) between 0900 and 1500 JST are shown in Fig. 3. These values were compared with typical values in SIGTOR (F2-F5 tornado damage) supercell environment in the United States reported in Thompson et al. 2003 (hereafter T03). The 1DVAR-derived MLCAPE increased significantly to about 1000 J kg^{-1} 1.5 hours before the occurrence of the tornado, although the value was smaller than the T03 values of 1059–3683 J kg^{-1}. A high MLCAPE before the approach of the supercell indicates the existence of environmental conditions favorable for the supercell. The SRH1km and SRH3km respectively attained maximum values of 170 and 260 m^2 s^{-2} for 1230–1250 JST. These vertical wind shear parameters are comparable to typical values, and indicate that a strong, low-level, vertical wind shear supports the SIGTOR supercell environment. The 1DVAR-derived STP also attained a maximum value of 1.2 at around 1250 JST, which was within the range of typical values, 0.5–6.3.

3. Conclusions and remarks

We used the 1DVAR technique to obtain close-proximity, high-frequency, probable soundings within the Tsukuba F3 tornadic supercell environment. The tornado forecast parameters obtained from 1DVAR-derived thermodynamic profiles indicated that the Tsukuba F3 tornadic event occurred under conditions associated with a SIGTOR supercell category. The results of this study also show that thermodynamic environments became unstable before the approach of the SIGTOR supercell and that low-level vertical wind shear changed locally near the supercell. The combination of high-frequency thermodynamic profiles retrieved from MWR data and wind profiler data would be of benefit in nowcasting severe storms such as SIGTOR supercells.
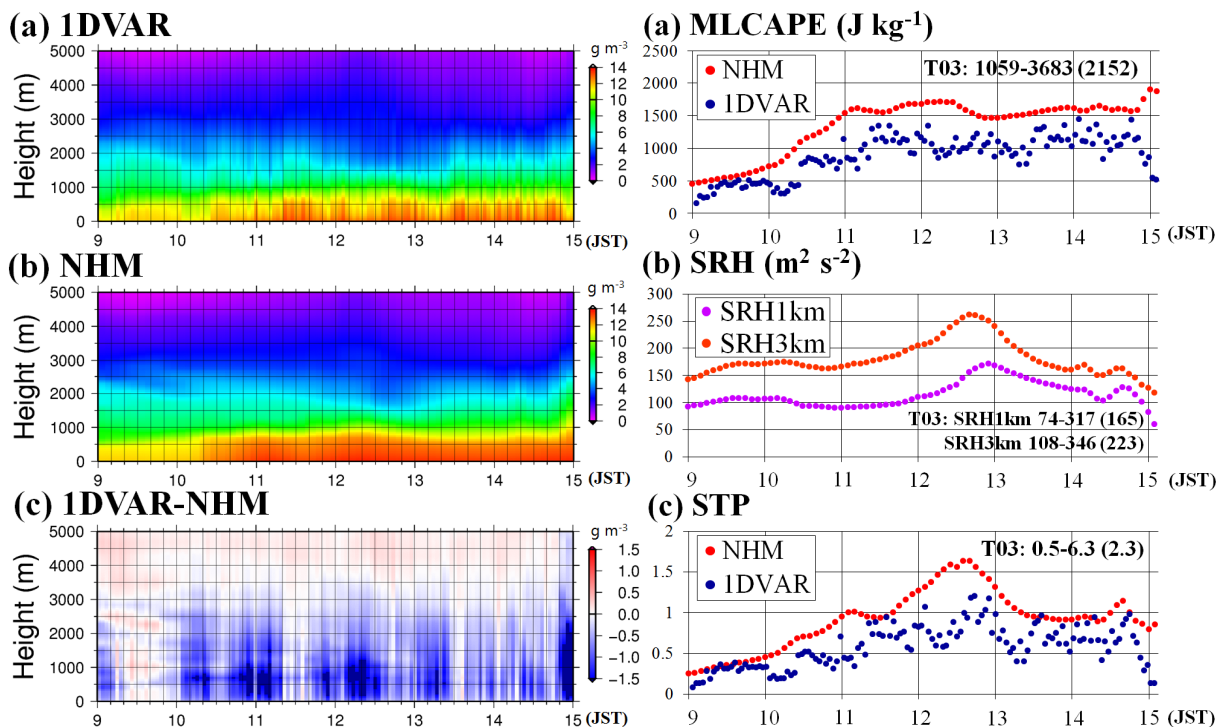

Figure 2. Time-height cross sections of (a) 1DVAR- and (b) NHM-derived water vapor density; and (c) the difference between (a) and (b).

Figure 3. Time series of parameters of (a) MLCAPE (b) SRH1km and SRH3km, and (c) STP. Numbers in each panel indicate the 10th and 90th percentiles, and the median (in parentheses) of each parameter in the SIGTOR supercell category reported by T03.

References:

Araki, K., H. Ishimoto, M. Murakami, and T. Tajiri, 2014: Temporal variation of close-proximity soundings within a tornadic supercell environment. *SOLA*, **10**, 57–61.

Araki, K., M. Murakami, H. Ishimoto, and T. Tajiri, 2015: The impact of ground-based microwave radiometer data to estimation of thermodynamic profiles in low-level troposphere. *CAS/JSC WGNE Research Activities in Atmospheric and Oceanic Modelling*, **45**.

Ishimoto, H., 2015: Analysis of microwave radiometric data using a 1DVAR technique. *Meteor. Res. Notes*, (in press, in Japanese).

Saito, K., T. Fujita, Y. Yamada, J. Ishida, Y. Kumagai, K. Aranami, S. Ohmori, R. Nagasawa, S. Kumagai, C. Muroi, T. Kato, H. Eito, and Y. Yamazaki, 2006: The operational JMA nonhydrostatic mesoscale model. *Mon. Wea. Rev.*, **134**, 1266–1298.

Thompson, R. L., R. Edwards, J. A. Hart, K. L. Elmore, and P. Markowski, 2003: Close proximity soundings within supercell environments obtained from the Rapid Update Cycle. *Wea. Forecasting*, **18**, 1243–1261.

The Impact of 3-Dimensional Data Assimilation using Dense Surface Observations on a Local Heavy Rainfall Event

Kentaro Araki, Hiromu Seko, Takuya Kawabata, and Kazuo Saito

Meteorological Research Institute, Tsukuba, Japan
e-mail: araki@mri-jma.go.jp

1. Introduction

Local heavy rainfalls (LHRs), which often cause disasters with loss of human life, are known to be caused by mesoscale convective systems (MCSs) composed of small-scale convective cells without synoptic forcing in warm seasons. In spite of recent progresses in numerical modeling and data assimilation, accurate prediction of such small-scale convective cells and LHRs remains challenges. To improve the forecasts of LHRs, it's required to understand the processes of convection initiation (CI) and preconvective environments where and when deep convective cells and MCSs develop.

On 9 August 2009, in the situation without synoptic forcing, a LHR event occurred in the Chiba city on the Kanto Plain in Japan and 3-hour accumulated rainfall by 1800 Japan Standard Time (JST; JST = UTC + 9 h) reached 150 mm (Fig. 3). The operational mesoscale model of the Japan Meteorological Agency (JMA) failed to predict the LHR. We performed a case study on mesoscale data assimilation using a surface network of JMA's Automated Meteorological Data Acquisition System (AMeDAS) with horizontal resolution of about 21 km and another dense surface observation network of the Atmospheric Environmental Regional Observation System (AEROS; Nishi et al. 2015) of the Japanese Ministry of Environment (Fig. 1). The AEROS ('Soramame' in Japanese) observes surface relative humidity in addition to air temperature and wind with a horizontal resolution of about 4–5 km in urban areas. The dense surface observation network revealed that a triple point (TP) was formed near the Chiba city (east of Tokyo) about 1.5 hours before the CI and triggered the CI at 1320 JST. Since convective cells initiated on the TP moved northeastward, where cold and moist northeasterly flow was observed at the surface, the TP was not likely affected by cold outflows from convective cells. As the result, the TP was maintained and caused the formation of a MCS and the LHR in the Chiba city.

2. Design of data assimilation

We performed numerical experiments by the JMA non-hydrostatic model (NHM; Saito et al. 2006). In the experiments, triply nested one-way grids (horizontal grid spacing of 20 km; 20km-NHM, 5 km; 5km-NHM and 2 km; NODA) were used. The initial and boundary conditions in 20km-NHM were provided by the JMA global analysis and results of JMA global spectrum model, respectively. Setups of the model were almost the same as in Saito et al. (2006), except that the Kain-Fritsch convective parameterization scheme was switched off in NODA.

In order to reproduce the preconvective environments in the initial field, the 3-dimensional variational assimilation system (JNoVA0; Miyoshi 2003) was also used in this study. The dense surface observations, which captured the TP triggering the CI, would be of benefit in predicting the CI and the LHR. The forecast of 5km-NHM from 1200 JST on the day was used as the first guess, and the initial fields were produced by assimilating surface observation data within a domain of 138–142°E and 34–37°N at 1200 JST; wind and temperature observed by AMeDAS, and wind, temperature, and relative humidity observed by AEROS. The horizontal resolution of the analysis was 5 km, and the observational error was set same as one of AMeDAS in JMA mesoscale analysis. Experiments with horizontal grid spacing of 2 km were performed by using the initial conditions provided by the JNoVA0 analyses using only AMeDAS data (AME) and AEROS and AMeDAS data (SORA). In SORA, relative humidity data only within the plain
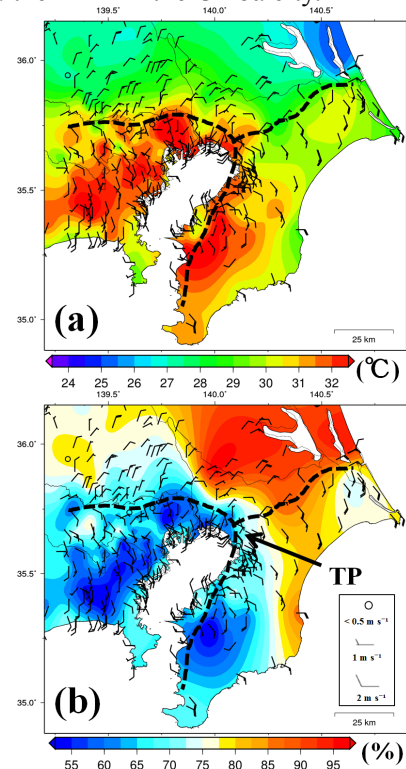

Figure 1. (a) Surface temperature and (b) relative humidity observed by the dense surface observation network at 1200 JST on 9 August 2009. A Barb indicates horizontal wind. Broken lines denote convergence lines.

regions of 139.5–141.2°E and 34.7–36.5°N were used, because the use of the relative humidity data in mountainous region tended to overestimate the water vapor in analysis.

3. Impact of data assimilation using dense surface observations

Figure 2 shows initial fields in NODA, AME, and SORA. Although the initial field in NODA reproduced a part of low-level convergence lines in the Kanto Plain, northeasterly flow in the north of the Chiba city was absent. On the other hand, the northeasterly flow was successfully analyzed in the initial fields in AME and SORA, and the convergence line in the west of the Chiba city was well produced in SORA. This result suggests that dense surface wind observations are necessary to analyze the detailed convergence structure in the lower troposphere. Although the surface temperature in urban areas in NODA was 3–4 °C lower than observations, the initial field in AME improved the horizontal distribution of temperature. The initial field in SORA also resolved the detailed temperature structures in urban areas. The initial field in SORA successfully analyzed high relative humidity in the north of the Chiba city, while NODA and AME did not reproduce the distribution.

As the result of NODA, the intense rainfalls were not reproduced at all (Fig. 3). In the experiments with initial field analyzed by using only wind of AMeDAS and Soramame, short-lived convective cells were appeared but observed MCS were not reproduced (not shown). On the other hand, the MCS was reproduced in the experiments with initial field analyzed by using temperature and wind such as AME, because the structure of temperature in urban areas maintained the convergence lines in the Kanto Plain. As the result of SORA, an LHR with 3-hour accumulated rainfall of 250 mm was reproduced in the Chiba city, and another LHR in the west of the Chiba city was also reproduced. This result indicates that data assimilation of low-level water vapor is important in predicting accurate location and amount of precipitation in LHR events.

In this study, dense surface observations including wind, temperature, and relative humidity were used for the data assimilation and the effect on reproducibility of a LHR event was investigated. The result showed that dense surface observations capturing the detailed preconvective environment of low-level convergence, temperature, water vapor fields, which were necessary for the CI and formation of the MCS, had an advantage in predicting an LHR event.

(a) Divergence (10^{-4} s^{-1})

(b) Temperature (℃)
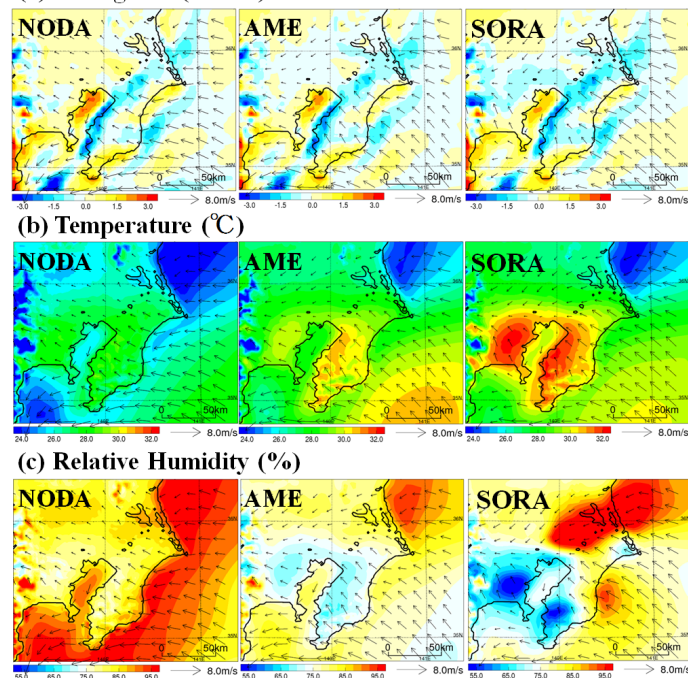
(c) Relative Humidity (%)

Figure 2. Initial fields of (a) horizontal divergence, (b) temperature, and (c) relative humidity of 20 m above the surface in each experiment. Vectors indicate horizontal wind at the same height.
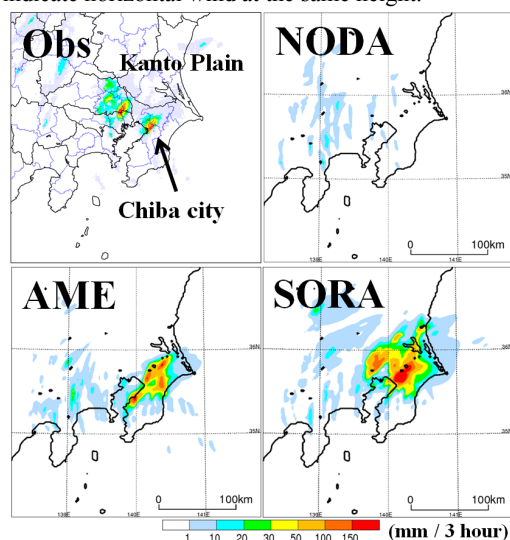

(mm / 3 hour)

Figure 3. Observed and simulated 3-hour accumulated rainfalls by 1800 JST.

References:

Miyoshi, T., 2003: Development of a 3-dimensional variational assimilation system (JNoVA0), *Annual report of the Numerical Prediction Division of JMA*, **49**, 148-155 (in Japanese).

Nishi, A. K. Araki, K. Saito, T. Kawabata and H. Seko, 2015: The characteristics of the Atmospheric Environmental Regional Observation System (AEROS) meteorological observation data. *Tenki.* (in Japanese with English abstract, in review)

Saito, K., T. Fujita, Y. Yamada, J. Ishida, Y. Kumagai, K. Aranami, S. Ohmori, R. Nagasawa, S. Kumagai, C. Muroi, T. Kato, H. Eito, and Y. Yamazaki, 2006: The operational JMA nonhydrostatic mesoscale model. *Mon. Wea. Rev.*, **134**, 1266–1298.

Improved representation of forecast error dynamics
using an increased size for ensemble 4D-Var data assimilation at Météo-France

Loïk Berre and Gérald Desroziers
CNRM-GAME, Météo-France and CNRS
42 avenue Coriolis 31057 Toulouse, France
loik.berre@meteo.fr

Assimilation of observations in numerical prediction models, such as the Météo-France global ARPEGE system, relies on accurate description of spatial correlations of forecast errors, as these allow observations to be spatialized. The estimation of these correlations is currently based on an ensemble data assimilation system containing 6 perturbed 4D-Var members and a temporal average over the 4 most recent days. This provides about one hundred forecasts in order to estimate correlations, which are recomputed once a day.

A new version of the ARPEGE ensemble 4D-Var assimilation has been developed, based on 25 members, a temporal average reduced to one day and a half (instead of 4 days), and an update of correlations every 6 hours (instead of 24 hours).

The figure illustrates that a more frequent update of correlations enables to account for the geographical variations of horizontal correlations length scales, estimated on 15 November 2013 at 06UTC and at 12UTC respectively. One can observe in particular that these length scales evolve significantly over 6 hours in this area, which is linked, among other things, to the displacement of low pressure systems.

Impact studies indicate that this improved representation of correlations, associated to the increase of ensemble size, allows improved forecast quality. This new version of the ensemble assimilation also allows the 35 members of the ARPEGE ensemble prediction system to be better initialized, by providing 25 independent initial perturbations.

These evolutions will be part of the version of the ARPEGE system which will be made operational in 2015.
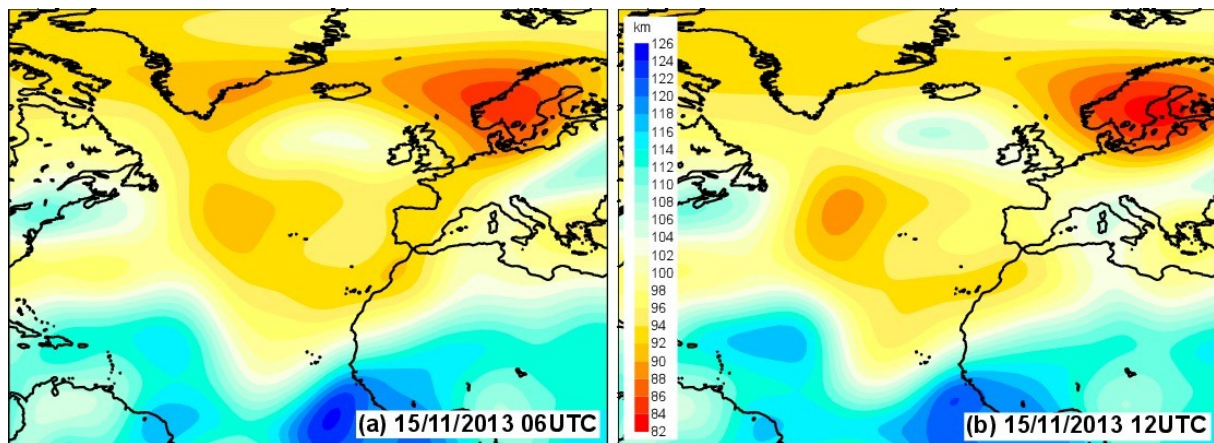
Figure 1 : Horizontal length scales of forecast correlations errors of wind near 300 hPa (9.2 km height, colour shading, in km), estimated 15 November 2013 at 06UTC (a) and at 12UTC (b). The length scale of a local correlation function is a measure of its spatial extension.

References :

Berre, L. and G. Desroziers, 2010: Filtering of Background Error Variances and Correlations by Local Spatial Averaging: A Review. Mon. Wea. Rev., 138, 3693-3720.

Berre, L., Varella, H., Desroziers, G. (2015), Modelling of flow-dependent ensemble-based background error correlations using a wavelet formulation in 4D-Var at Météo-France. Submitted to Q.J.R. Meteorol. Soc.

Fisher, M., 2003: Background error covariance modeling. Proc. ECMWF Seminar on "Recent Developments in Data Assimilation for Atmosphere and Ocean", 8-12 Sept 2003, Reading, U.K., 45-63.

Varella, H., Berre, L. and Desroziers, G. (2011), Diagnostic and impact studies of a wavelet formulation of background-error correlations in a global model. Q.J.R. Meteorol. Soc., 137: 1369–1379. doi: 10.1002/qj.845

A technology to prepare initial fields of snow water equivalent and snow density for atmospheric models

Ekaterina Kazakova, Mikhail Chumakov, Inna Rozinkina

Hydrometcenter of Russia, Russia

kaza4ok-87@mail.ru, inna.rozinkina@mail.ru

Snow analysis done at different meteorological centers is usually based on SYNOP snow depth measurements and satellite data about snow fractional cover. Other measurements of snow cover characteristics are carried out (aircraft measurements, snow surveys, measurements at automatic meteorological stations, etc.), but because of their temporal and spatial resolution these data can be used only for some special tasks and are not suitable for operational forecasting technologies. The problem is that NWP models need snow water equivalent (SWE) and snow density data as input. SWE can be restored from the snow depth based on the snow density usually calculated by simple formulas or assumed constant. All this leads to discrepancies in the initial SWE and snow density fields. As it was demonstrated in our study, these discrepancies can be very large - the SWE fields routinely used in COSMO model differed by a factor of up to 2 from snow surveys' data in Russia [1].

In order to calculate SWE and snow density a new multi-layer snow model was created at the Hydrometcenter of Russia [2]. It is sketched in Fig.1. The model uses only standard SYNOP station data for input thus enabling daily calculations during the whole snow period. SWE values calculated by the snow model were in good correspondence with snow surveys' measurements done in the European part of Russia [2].
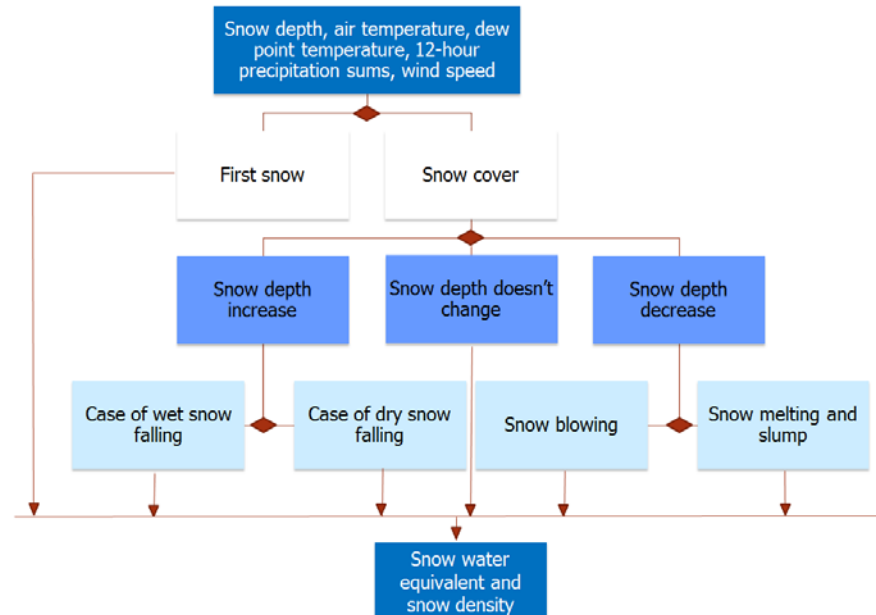

Fig.1. Scheme of the multi-layer snow model

Based on the snow model, a technology for preparation of initial fields of SWE and snow density was proposed. It has been implemented in experimental mode since the end of 2014 (Fig.2). 78-h forecasts using new SWE and snow density are issued daily for 00 UTC for the two domains of COSMO model in Russia - Europe (COSMO-Ru7 with a resolution of 7 km) and Central Russia (COSMO-Ru2 with a resolution of 2,2 km).
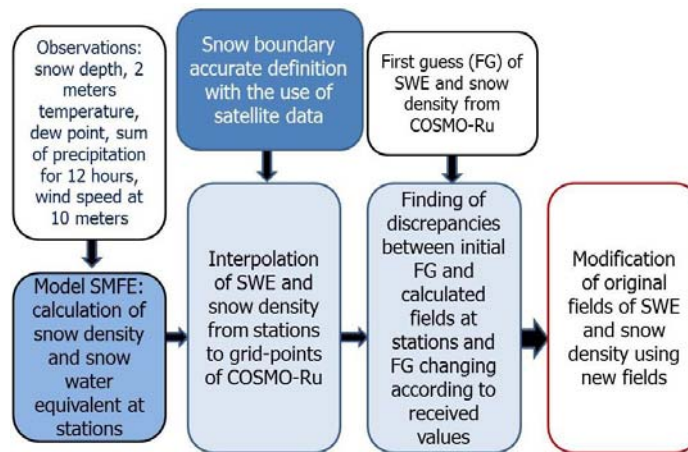
Fig.2. Scheme of the technology for preparation of initial fields of SWE and snow density at the Hydrometcenter of Russia

The introduction of the new technology led to maximum changes in meteorological elements in a zone close to the snow boundary during the snow period. The effect was most prominent during snow melting and for air temperature.

Figure 3 demonstrates an improvement of the forecast skill due to implementation of the new technology (for cases when positive temperatures are observed at stations). The air temperature ME and RMSE clearly decreased over Europe, especially for the third forecast day.
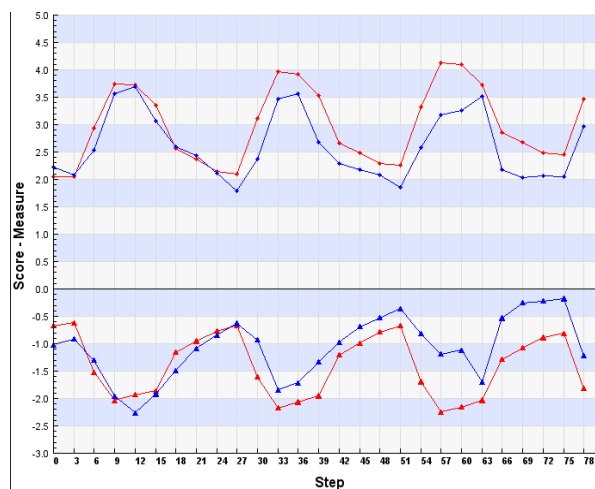
Fig.3. The air temperature ME (bottom panel) and RMSE (upper panel) over Europe for COSMO-Ru7 operational forecasts (red) and for the forecasts made using the new technology (blue). 24 Feb – 31 March 2015

Changes in COSMO-model forecasts of 10-meter wind speed, surface albedo and cloudiness are also found.

References

1. Kazakova E., Rozinkina I. Testing of Snow Parameterization Schemes in COSMO-Ru: Analysis and Results // COSMO Newsletter No.11, 2011, pp.41-51
2. Kazakova E., Chumakov M., Rozinkina I. Realization of the parametric snow cover model SMFE for snow characteristics calculation according to standard net meteorological observations // COSMO Newsletter No.13, 2013, pp.39-49

Improvement of snow analysis using an offline land-surface model

Hiroshi Kusabiraki

Numerical Prediction Division, Japan Meteorological Agency, Japan
hiro.kusabiraki@met.kishou.go.jp

1 Introduction

Land-surface conditions and their initialization significantly affect the accuracy of lower-atmosphere variables in numerical weather prediction models. In particular, the presence or absence of ground snow cover is a critical factor because the significantly lower heat capacity of snow can have a great impact on near-surface temperatures, especially under clear-sky conditions when radiative cooling is dominant.

In the JMA's operational regional Meso Scale Model (MSM) with 5-km horizontal grid spacing, information on the status of ground snow cover is provided via a snow analysis system. As the results of snow cover analysis remain unchanged during the forecast period, the current model cannot incorporate consideration of increasing or decreasing snow extents.

Our verification revealed that inaccurate, overspread snow cover often causes significant errors in near-surface temperature forecasting during winter night-time (known as "runaway cooling") in the MSM. To address this problem, the snow analysis system was updated in November 2014. The new system employs an offline land surface model called eSiB to generate the first guess (background field) of snow depth distribution, which is used to estimate the snow cover extent. This report gives a brief overview of the new system and its impacts on MSM accuracy.

2 New snow analysis method

Figure 1 shows schematic diagrams of the old and new snow analysis systems. In the old system, snow depth distribution data offered by the JMA's Global snow depth analysis (with 1 x 1-degree grid spacing) were modified using observations from ground station reports. Our investigation revealed that snow cover results from Global snow analysis tended to be overestimated, especially in regions where observation stations are sparsely distributed. Excessive snow cover results were a major source of near-surface temperature forecast errors associated with runaway cooling.

To reduce these errors, the new snow analysis method employs a higher-resolution two-dimensional optimum interpolation system (2D-OI) in which snow depth first guesses (FGs) are estimated by an offline version of the land-surface model (Offline-LSM) with the same domain and grid spacing as the MSM.
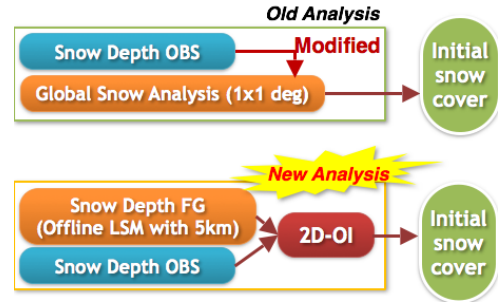

Figure 1: Snow analysis flow-charts comparing old and new
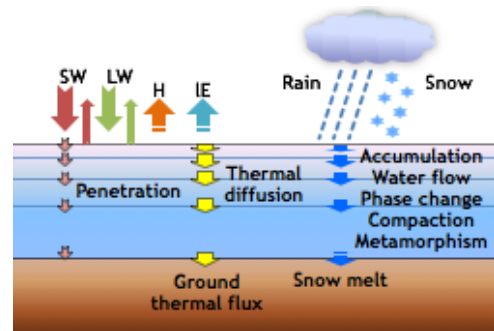

Figure 2: A schematic diagram of a multi layer snow model in eSiB (Kusabiraki, 2013).

The offline LSM (eSiB; Kusabiraki, 2013), which includes a multi-layer snowpack model, simulates typical snow processes such as accumulation and ablation (Figure 2). Temperature and wind velocity at the lowest atmospheric level and radiative flux toward the surface as predicted by the MSM are provided to eSiB for atmospheric forcing as necessary in order to drive the LSM. Radar/Raingauge-Analyzed Precipitation data [1] are also provided for forcing.

The snow depth predicted using eSiB and observations made through SYNOP and AWS facilities in Japan (AMeDAS; Automated Meteorological Data Acquisition System) are handed over to the 2D-OI system. The standard deviations of observation and background errors are set at 4 and 3 cm, respectively. The methodology of OI (e.g., formulation of horizontal correlation) is based on Brasnett (1999), where the horizontal and vertical length parameters ($1/c$ and h; see Eqs.(5) and (6) in Brasnett, 1999) are set to 25 km and 500 m, respectively.

---

[1] http://www.jma.go.jp/jma/jma-eng/jma-center/rsmc-hp-pub-eg/techrev/text13-2.pdf

Grid squares with an analysis-based snow depth greater than 5 cm are classified as snow-covered ground. In the next running of eSiB, initial values of snow water equivalent are estimated from analyzed snow depth and snow density in the previous run so that snow amounts in eSiB are consistent with analysis-based snow depth fields.

3   Results

The results of experimentation conducted to evaluate the impacts of the new snow analysis method show improvement of predicted screen-level temperature in the MSM. Figure 3 shows snow cover extents determined from the old (OLD; left) and new (NEW; right) analysis for 14 January 2014 over Japan's Hokuriku region. The new analysis provides much finer definition of snow cover extents because forecasts from eSiB are used as the FG instead of coarser snow analysis. Figure 4 shows the impact of more accurate snow cover analysis on screen level temperature prediction. The old analysis represents the snow cover area near the Fukui ground station point (indicated by blue arrows in Figure 3). MSM with snow cover initialized via the old snow analysis system (the green line in Figure 4) produces significantly lower screen-level temperature than the Fukui observation station data (the black line in Figure 4) at nighttime. Meanwhile, with snow cover information provided by the new snow analysis system, the predicted screen-level temperature is much closer to the corresponding observation. It can be concluded that the new snow analysis approach supports the generation of more realistic fields of snow cover and results in more accurate screen level temperature prediction.

A look at statistical errors calculated from a large number of samples also illustrates the accuracy improvement achieved. Figure 5 shows mean errors of the MSM with snow cover initialized using the old and new snow analysis methods (denoted as CNTL and TEST, respectively). While forecasts based on the new configuration still have cold biases at nighttime, these are reduced in TEST (indicated by red lines) against CNTL (green lines), and the root mean square errors (RMSE) in TEST are also reduced in comparison to CNTL (not shown). These figures illustrate that the new snow analysis method produces better determination of snow cover extents and screen-level temperature forecasts.

References

Brasnett, B., 1999: A global analysis of snow depth for numerical weather prediction. *J. Appl. Meteor.*, **38**, 726–740.

Kusabiraki, H., 2013: Offline validation of a multi-layer snow scheme for a new land surface model in the operational regional NWP model at JMA. *13th EMS Annual Meeting and 11th European Conference on Applications of Meteorology, Reading, United Kingdom.*
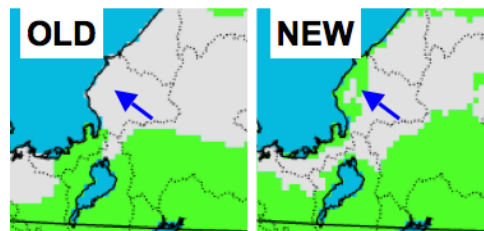
Figure 3: Example of analysis-based snow cover extents from the old and new snow analysis systems for Japan's Hokuriku region on 14 January 2014. White shading indicates snow-covered areas. Fukui ground observation station is denoted by blue arrows.
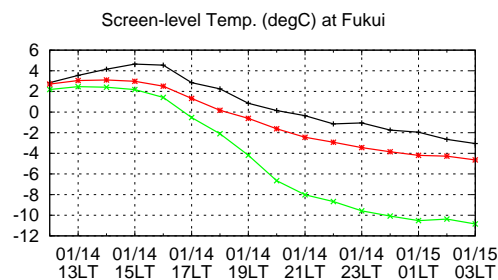

Figure 4: Time-series representation of screen-level temperature at Fukui. The red line shows forecasts of the MSM with the new snow analysis method (corresponding to the right side of Figure 3), and the green line shows that of the MSM with the old method (corresponding to the left side of Figure 3). The black line shows observations at Fukui. The x-axis shows the localtime (LT; UTC+9hrs).
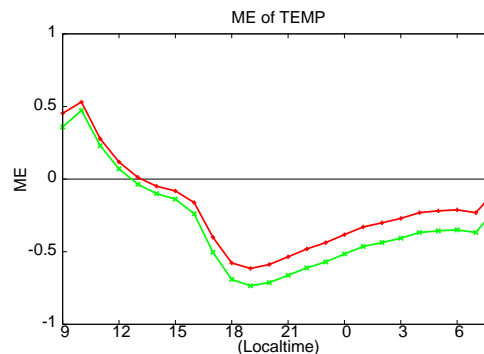

Figure 5: Time-series representation of mean errors in screen-level temperature forecasts. The green line shows CNTL results (MSM forecast with OLD), and the red line shows TEST results (MSM forecast with NEW). Statistics are computed based on AWS observations (about 300 points) for the period from 8 January to 28 February 2014. The x-axis shows the localtime (UTC+9hrs).

Assimilation of FY-3 MWTS radiance data into Chinese NWP systems

Li, Juan[1] and Xiaolei Zou[2]

[1] Numerical Weather Prediction Center, China Meteorological Administration

[2] Department of Atmospheric sciences, Nanjing University of Information Science & Technology

E-mail: lj@cma.gov.cn

1. Introduction

Chinese Fengyun-3A (FY-3A) satellite was successfully launched on 27 May, 2008. The Microwave Temperature Sounder (MWTS) onboard FY-3A is the first microwave sounding unit in China. The second in the FY-3 series, FY-3B, was successfully launched on November 5, 2010, carrying the same instruments as those on board FY-3A. On September, 23, 2013, the satellite FY-3C was launched. The MWTS onboard FY-3A/B has four channels that are similar to AMSU-A channels 3, 5, 7, and 9 and provide atmospheric temperature sounding. The microwave sounding unit onboard FY-3C has thirteen channels that are similar to SNPP ATMS temperature sounding channels. This report details the quality control (QC) scheme and the impacts on Numerical Weather Prediction (NWP) system.

2. Quality Control scheme

To assimilate these MWTS radiances into NWP system, a cloud detection scheme is needed. Currently, there are several cloud detection methods developed for microwave satellite measurements (eg: AMSU-A). However, the two surface-sensitive channels (23.8 GHz and 31.4 GHz) used in the existing cloud detection schemes are not available from the MWTS onboard FY-3A/B/C satellite. These algorithms developed for the AMSU-A data cannot be directly applied to the MWTS observations.

A new cloud detection algorithm is proposed for the MWTS (Li and Zou, 2013). The method is based on the cloud fraction product provided by the Visible and InfrarRed Radiometer (VIRR) onboard FY-3 satellites. A MWTS field-of-view (FOV) with a cloud fraction greater than a threshold f_{VIRR} will be identified as a cloudy radiance. The threshold f_{VIRR} is determined by the AMSU-A cloud liquid water path products, obtained from the Microwave Surface and Precipitation Products System (MSPPS). Analysis of the test results indicates that most clouds are identifiable by applying a VIRR cloud fraction threshold of 76%.

Other QC steps for FY-3A/B/C MWTS include the following: (i) two (for FY-3A/B) or eight (for FY-3C) outmost FOVs; (ii) measurements from low level channels over sea ice and land; (iii) coastal FOVs; and (v) outliers with large differences between model simulations and observations. In addition, another step is needed for FY-3C MWTS. The differences between brightness temperature observations and simulated observations based on numerical weather predictions, i.e., O-B, exhibit a clear striping pattern. We use the PCA+EEMD method to remove the striping noise. Firstly, the principal component analysis is applied to isolate scan-dependent features such as the cross-track striping from the atmospheric signal. Secondly, an Ensemble Empirical Mode Decomposition (EEMD) is used to extract the striping noise. When the noise is removed from the data, the striping noise is imperceptible in the global distribution of O-B for FY-3C MWTS sounding channels.

3. Impacts on the global NWP system

The impact of MWTS radiances on the prediction of Chinese NWP system GRAPES (Global and Regional Assimilation and Prediction System) was researched. Both typhoon case study and cycle experiments were conducted. The typhoon case study shows that the assimilation of MWTS data can improve the typhoon track prediction by changing the model-predicted steering flow. The impact cycle experiments conducted for 30-day periods show that the QC scheme removed the outliers efficiently. Verifications indicate that forecast skill is improved after assimilating MWTS data.

4. Plans

The FY series is becoming an increasingly important component of the global observing system. The applications of these measurements have also been researched in ECMWF and UKMO. Currently, a telecommunication conference on the improved assimilation of FY satellite data among CMA/NSMC (National Satellite Meteorological Centre), CMA/NWPC (Numerical Weather Prediction Center), UKMO and ECMWF, was held regularly. The conference is proved to be a very efficient and economical means of communicating the findings between the four centers.

In the near future, plans are made to assimilate Microwave Humidity and Temperature Sounder (MWHTS) and FY-3D microwave sounder data in a new version of the operational GRAPES. More details on the MWTS impact evaluation can be found in Li, et al., 2015.

References:

Li Juan, X. Zou, 2013: A quality control procedure for FY-3A MWTS measurements with emphasis on cloud detection using VIRR cloud fraction. *J. Ocean Atmos. Tech*., **30**, 1704–1715.

Li Juan, X. Zou and G. Liu, 2015: Assimilation of Chinese FengYun 3B Microwave Temperature Sounder radiances into global GRAPES system with an improved cloud detection threshold. *Frontiers of Earth Science*, Accepted.

Qin Zhengkun, X. Zou and F. Weng, 2013: Analysis of ATMS striping noise from its Earth scene observations. *J. Geophys. Res.*, **118**(13), 13214-13229.
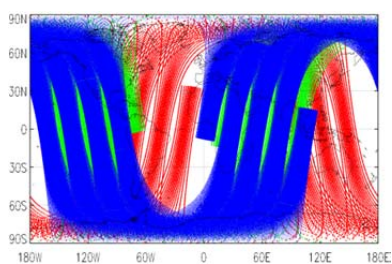
Fig.1: Data coverage of MWTS from FY-3A (green) on 0300 UTC-0900 UTC July 1, 2012, FY-3B (red) on 0300 UTC-0900 UTC July 1, 2013 and FY-3C (blue) on 0300 UTC-0900 UTC July 1, 2014.
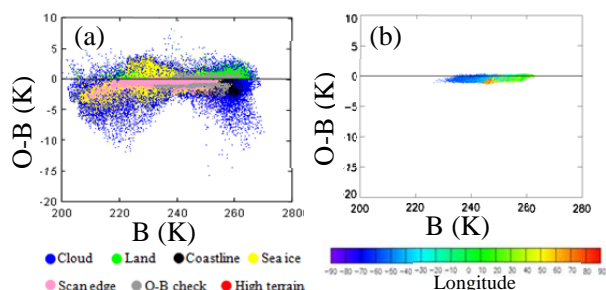

Fig.2: Scatter plots of the differences of brightness temperature between observations and model simulations for FY-3A MWTS channel 2 (a) outliers and (b) data that pass quality control during 1-5 July 2011.

Assimilation of IASI and AIRS radiances at JMA

Akira Okagaki

Numerical Prediction Division, Japan Meteorological Agency

Email : a-okagaki@met.kishou.go.jp

1. Introduction

Observations from the Infrared Atmospheric Sounding Interferometer (IASI) and the Atmospheric Infrared Sounder (AIRS) have been operationally assimilated into JMA's global Numerical Weather Prediction (NWP) model since 4 September 2014. Only radiances unaffected by cloud are assimilated. This report briefly outlines the usage of these data at JMA and impacts on NWP quality.

2. Data and channel selection

IASI is a Michelson interferometer with 8,461 channels covering the infrared spectral domain (3.5 – 15.5μm). The first IASI was launched on EUMETSAT's Metop-A satellite in October 2006 and its successor was launched on the Metop-B satellite in September 2012. AIRS is a grating spectrometer with 2,378 channels covering a domain similar to that of IASI. It was launched on NASA's Aqua satellite in May 2002. These high spectral resolution sounders are capable of providing information on atmospheric temperature and humidity with high vertical resolution.

JMA utilizes the IASI dataset consisting of 616 channels spatially thinned to one pixel from four for each scan position, and the AIRS dataset consisting of 324 channels spatially thinned to one from nine for each scan position. Long-wave temperature sounding channels (around 15 μm) were selected as assimilation targets to improve the accuracy of the temperature field in analysis. There are 69 selected channels for IASI and 76 for AIRS. For AIRS, 9 channels around 4.4 μm are added only in the nighttime.

3. Quality control

Quality control (QC) for IASI and AIRS involves quality-flag checking, gross checking and cloud checking. Treatment of cloud is essential in comparing infrared observation and forecast models in the troposphere. Cloud contaminated observations are excluded to avoid the complexity of having to consider the effects of cloud in data assimilation.

Cloud checking is applied for each field of view over the ocean. It involves cloud detection based on the difference between observed radiance and simulated radiance assuming clear sky in the window channel, and cirrus detection based on the difference between observed radiance in the 11 and 12 μm channels. When cirrus is detected, a cloud top height is assigned at the tropopause height. When cloud other than cirrus is detected, the cloud top height is estimated using the minimum residual method (Eyre and Menzel 1989). Channels sensitive to the atmosphere below the estimated cloud top are excluded because they could be affected by cloud, while others are flagged as clear. Figure 1 shows histograms of the first-guess (FG) departure of IASI lower-tropospheric channels for all and clear-flagged data. The normal distribution curve for clear-flagged data indicates that cloud checking appropriately screens out cloud-contaminated observations. All channels sensitive to the troposphere are excluded over land or sea ice.

4. Verification results

A pre-operational experiment was conducted to evaluate the impact of IASI and AIRS assimilation. The trial period covered a total of six months from July to September 2013 (JAS) and

from December to February 2013/2014 (DJF). Observations from IASI onboard Metop-A/Metop-B, and AIRS were additionally assimilated into the JMA operational global model in April 2014. Figure 2 shows that the root mean square (RMS) of FG departure for AMSU-A and MHS is reduced by the introduction of IASI and AIRS. This indicates accuracy improvement for temperature fields in the analysis and the first guess. Errors also exhibit a statistically significant reduction in short-range forecasting (Figure 3).

References

Eyre, J. R. and W. P. Menzel, 1989: Retrieval of Cloud Parameters from Satellite Sounder Data: A Simulation Study. J. Appl. Meteor. Climat., 267 – 275.
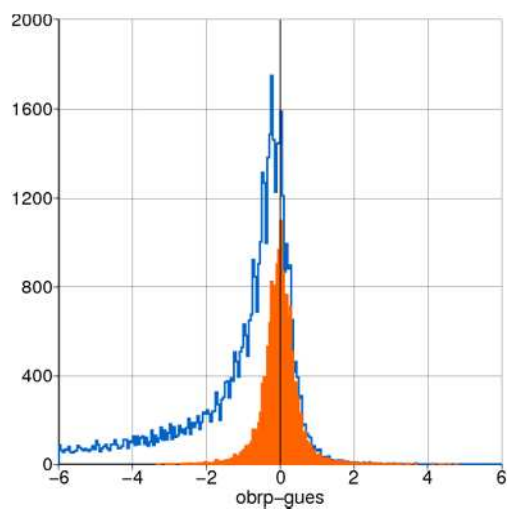
Figure 1. Histograms of FG departure [K] for MetopB/IASI lower-tropospheric channels. Blue: all data; Red: clear-flagged data in QC.
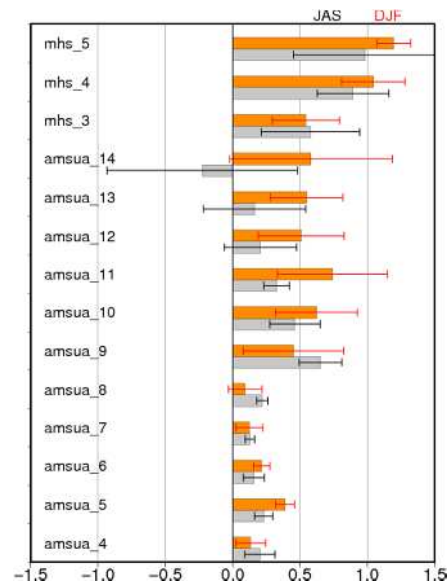

Figure 2. Normalized difference of RMS [%] in FG departure for AMSU-A channels 4 − 14 and MHS channels 3 − 5. Gray bars show the JAS period, and red bars show DJF. Positive values correspond to reduced RMS with IASI and AIRS assimilation. Error bars show a 95% confidence interval.
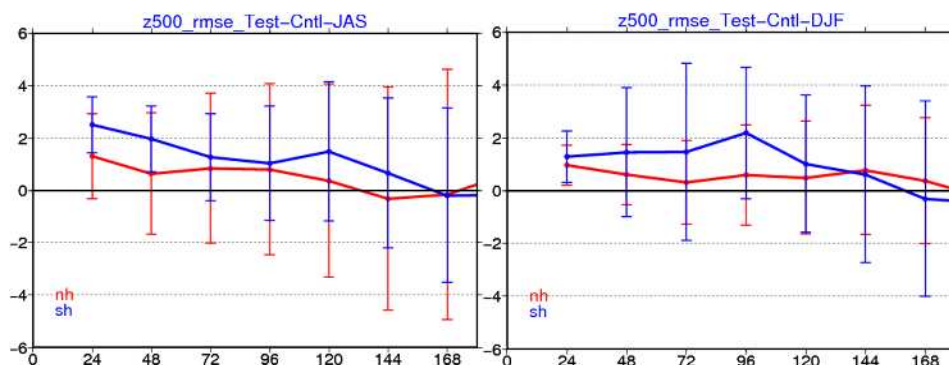

Figure 3. Normalized differences of RMS [%] in forecast errors for 500-hPa geopotential height verified against initial fields as a function of forecast range [hours]. Positive values correspond to reduced RMS with IASI and AIRS assimilation. Left: JAS period; Right: DJF period. Red lines show verification results for the northern hemisphere (20N − 90N), and blue lines show those for the southern hemisphere (90S − 20S). Error bars show a 95% confidence interval.

Preliminary results of assimilation of reflectivities of space-borne precipitation radars

[*1]Kozo Okamoto, [1]Kazumasa Aonashi, [2]Takuji Kubota and [3]Tomoko Tashima

[1]Meteorological Research Institute (MRI) of JMA
[2]Japan Aerospace Exploration Agency (JAXA)
[3]Remote Sensing Technology Center of Japan (RESTEC)
[*]e-mail: kokamoto@mri-jma.go.jp

1. Background

Space-borne precipitation radars, such as precipitation radar (PR) on the Tropical Rainfall Measurement Mission (TRMM) satellite and dual-frequency precipitation radar (DPR) on the Global Precipitation Measurement (GPM) Core satellite, measure accurate vertical precipitation profiles over both land and sea. This information is valuable for numerical weather prediction (NWP) because it complements ground-based radars and microwave imagers (MWIs). Aonashi and Eito (2011) have developed an ensemble-based variational (EnVA) scheme using a cloud-resolving model (CRM) and demonstrated that assimilation of precipitation-affected brightness temperature (BT) from MWIs improved precipitation forecasts. We improved EnVA by incorporating a radar simulator to assimilate radar reflectivity factors (Ze) and developed pre-processing for Ze. Preliminary results of TRMM/PR Ze assimilation are presented in this paper.

2. Model comparison

To understand the characteristics of models and Ze observations, we compared them in the attenuation-corrected Ze space. We employed the non-hydrostatic model (NHM) of the Japan Meteorological Agency (JMA) (JMA-NHM; Saito et al. 2004) as a CRM and the multi-satellite simulator called Joint-simulator (Hashino et al. 2013) as a radar simulator. The JMA-NHM in this study adopts a bulk microphysical scheme with two-moments for three ice species and is run with 5 km horizontal resolution in a region of 401×401 grids.

Figure 1 is a contoured frequency by altitude diagram (CFAD) showing a comparison between observation and the JMA-NHM ensemble forecast mean, which is used as the first-guess (FG) of data assimilation, for typhoon Conson at 22 UTC, June 9, 2004. It shows that the JMA-NHM significantly overestimates strong Ze from ice particles above the melting layer at approximately 5 km. This outcome is attributed to overestimating the population of large ice particles. For liquid–particle scattering, the frequency peak is located at modest Ze from 24 to 30 dBZ for observation and at lower Ze for FG. This inconsistency is related to displacement error of the rain band in the model simulation, as shown in Fig. 2, where the rain-mixing ratio (Qr) is overestimated in Area A and underestimated in Area B.

3. Assimilation of TRMM/PR Ze

We included the Joint-simulator as an observation operator for Ze in EnVA. For the initial implementation of assimilating Ze, we developed conservative quality-control (QC) procedures. Using these procedures, we excluded those observations in and above the melting layer, those affected by ground clutter, those having larger departure from FG, those with isolated rain signal in the vertical profile, or those with both observed and FG values less than the minimum value (17 dBZ). Furthermore, observations are thinned at every other angle bin and scan pixel for more optimal minimization and to reduce computational burdens.

We carried out three assimilation experiments to examine Ze assimilation performance in EnVA: (1) the "PRonly" experiment, in which PR Ze alone is assimilated; (2) the "TMIonly" experiment, in which TB of four vertical polarized channels at 19, 21, 37, and 85 GHz from the TRMM Microwave Imager (TMI) is assimilated, as in Aonashi and Eito (2011), and (3) the "PR+TMI" experiment, in which both PR Ze and TMI TB are assimilated. Figure 3 shows the analysis and its increment (analysis minus FG) for Qr at 2.5 km. All of these experiments successfully correct Qr to reduce the difference between observation and FG, as shown in Figs. 3 (b, d and f). The PRonly experiment, however, generates an analysis increment in a very limited area that corresponds to the PR observation coverage, resulting in an unnatural structure of the analyzed typhoon (Fig. 3 (a)). Both the TMIonly and the TMI+PR experiments produce wider analysis increments, as shown in Figs. 3 (d and f), because TMI has
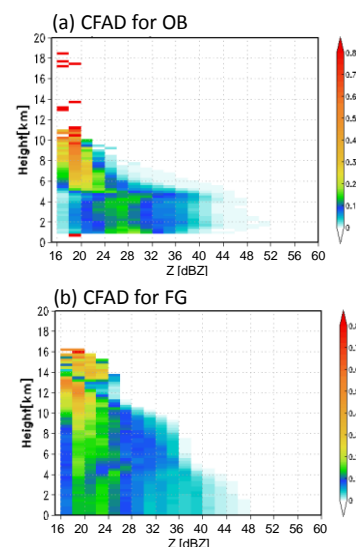

Fig. 1. CFAD of (a) observation (OB) of TRMM/PR and (b) first-guess (FG) from 7-hour ensemble forecast mean of JMA-NHM initialized at 15 UTC on June 9, 2004.
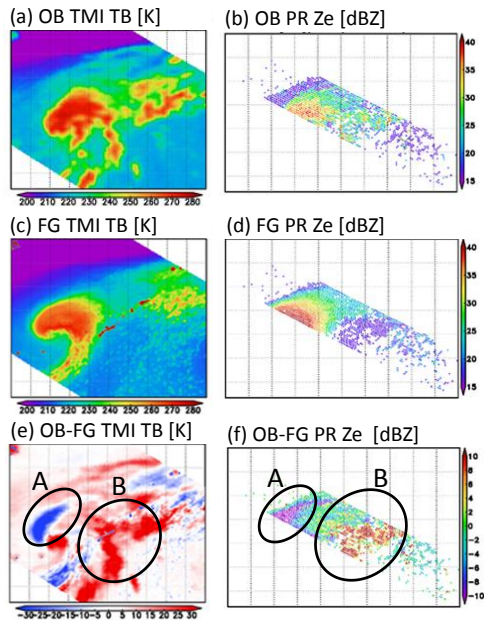
Fig. 2. (a, c, and e) observation (OB), first-guess (FG), and their difference of TB (Kelvin) of vertically polarized channel at 19 GHz (TB19V) from TMI. (b, d, and e) as in (a, c, and e) but for PR Ze (dBZ) at 2.5 km.

Fig. 3. Analyzed Qr (g/kg) at 2.5 km (AN) and its departure from first-guess (AN-FG) for three experiments.

a much wider scan-swath width of 878 km than the PR scan-swath width of 240 km. The TMI+PR experiment creates a slightly finer analysis increment than the TMIonly experiment because of smaller PR pixels.

The quality of the analysis with respect to the agreement with observations of TMI TB and PR Ze is summarized in Fig. 4. Large mean and standard deviations in TB for the PRonly experiment suggest that PR mainly corrects Qr to draw analysis to PR but has little impact on large-scale variables related to TB, such as humidity and temperature. This is confirmed by the analysis increment of these variables (not shown) and is explained by the fact that in EnVA control variables related to Qr have small correlation with the large-scale variables. In contrast, the analyses for TMIonly and TMI+PR experiments are in better agreement with TB and comparably fit Ze. A relatively large negative mean difference of Ze in the TMIonly experiment indicates that the TMI+PR experiment makes a more balanced analysis than the TMIonly experiment.

Fig. 4. Mean and standard deviation of OB-FG and OB-AN for three experiments with respect to TB19V and PR Ze.

4. Summary and Plans

We compared observed Ze and its model counterpart and found several deficiencies in the cloud microphysics in the JMA-NHM. Based on these findings, we developed QC procedures for Ze in EnVA. Assimilation experiments showed the importance of synergetic use of PR and TMI and the possibility to better analyze Qr. To further evaluate impacts of space-borne radars, we plan to make forecasts from the analysis made by assimilating Ze. Assimilation of DPR Ze is also under development.

Acknowledgements

References

Aonashi, K., and H. Eito, 2011: Displaced ensemble variational assimilation method to incorporate microwave imager brightness temperatures into a cloud-resolving model. *J. Meteor. Soc. Japan*, **89**, 175-194.

Hashino, T., M. Satoh, Y. Hagihara, T. Kubota, T. Matsui, T. Nasuno, and H. Okamoto, 2013: Evaluating cloud microphysics from NICAM against CloudSat and CALIPSO, *J. Geophys. Res. Atmos.*, **118**, 7273-7292, doi:10.1002/jgrd.50564.

Saito, K., T. Fujita, Y. Yamada, J. Ishida, Y. Kumagai, K. Aranami, S. Ohmori, R. Nagasawa, S. Kumagai, C. Muroi, T. Kato, H. Eito, and Y. Yamasaki, 2006: The operational JMA non-hydrostatic model. *Mon. Wea. Rev.,* **134**, 1266-1298.
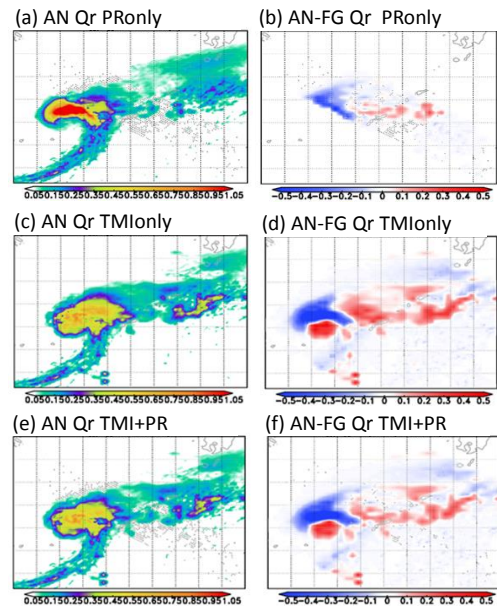
Recent updates on the use of GNSS RO data in JMA's Operational Global Data Assimilation System

Hiromi Owada and Masami Moriya

Numerical Prediction Division, Japan Meteorological Agency

E-mail: howada@met.kishou.go.jp

1. Introduction

Global Navigation Satellite System (GNSS) Radio Occultation (RO) observation is a very important component of the global observing system because it provides atmospheric vertical profile information and can be assimilated into numerical weather prediction (NWP) systems. The Japan Meteorological Agency (JMA) began assimilation of RO refractivity data into its global NWP system in March 2007, resulting in the improvement of analysis and forecast fields in the Southern Hemisphere and elsewhere. However, due to the well-documented degradation of retrieval precision, refractivity profiles cannot be assimilated at levels higher than 30 km. As the assimilation of bending angle profiles helps to avoid such assimilation height limitations, a new configuration for bending angle data assimilation was developed and tested. It was incorporated into the global NWP system on March 18, 2014.

2. Updates and related impacts

In the new configuration for bending angle assimilation, changes are applied to RO data preprocessing. By way of example, bending angle profiles above 30 km are not excluded, and vertical data thinning is removed because the vertical correlation of observation errors in bending angle profiles is small (Rennie 2010).

A one-dimensional observation operator provided as part of the Radio Occultation Processing Package (ROPP) was introduced for bending angle data assimilation. ROPP is developed and maintained by the Radio Occultation Meteorology Satellite Application Facility (ROM-SAF).

Observing system experiments were performed for the two months of August 2013 and January 2014 to identify the impact of RO data assimilation in the global NWP system. The experiment on bending angle assimilation (BANGLE) corresponding to the current operational configuration included the above-mentioned changes, and the experiment on refractivity assimilation (REFRAC) was identical to BANGLE except that refractivity data were assimilated with the previous operational configuration in place of bending angle data. The experiment which removed RO data assimilation from BANGLE (NO RO) was also conducted.

Figures 1 and 2 show the mean error and root mean square error of background (six-hour forecast) fit to radiosonde temperature measurements in the Northern Hemisphere for BANGLE, REFRAC and NO RO. It is clear that in both BANGLE and REFRAC, there was a reduction of large biases relative to radiosonde observations that appeared in the upper troposphere and stratosphere in the case of NO RO.

Figure 3 shows a time-series representation of the global averaged O-B (Observation before bias correction minus Background) for Metop-B/AMSU-A channel 13 during the initial 32 days of BANGLE, REFRAC and NO RO. The O-B of BANGLE was smaller than those of REFRAC and NO RO in all cases. As the weighting function for AMSU-A channel 13 peaks near 5 hPa, the background of BANGLE near 5 hPa was improved by assimilating RO profiles above 30 km.

Acknowledgements

References

Rennie, M. P., 2010: The impact of GPS radio occultation assimilation at the Met Office. *Quart. J. Roy. Meteor. Soc.,* 136, 116 – 131.
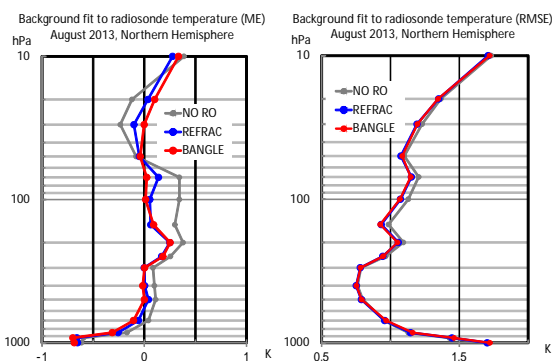
Figure 1: Mean error and root mean square error of background (six-hour forecast) fit to radiosonde temperature measurements in the Northern Hemisphere for bending angle assimilation (BANGLE; red line), refractivity assimilation (REFRAC; blue line) and removal of RO data assimilation (NO RO; gray line) experiments conducted in August 2013
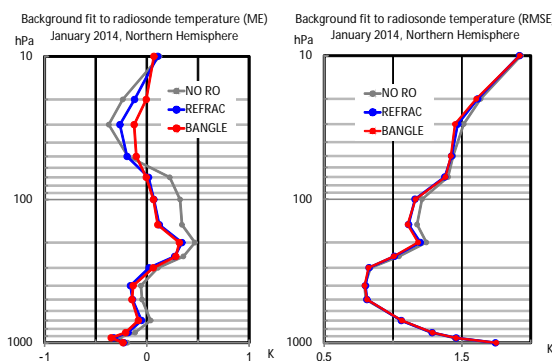
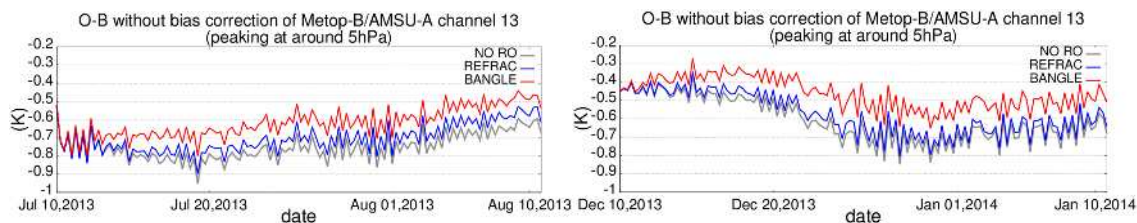Figure 2: As per Figure 1, but for January 2014

Figure 3: Time-series representation of global averaged O-B (Observation before bias correction minus Background) for Metop-B/AMSU-A channel 13 during the initial 32 days of bending angle assimilation (BANGLE; red), refractivity assimilation (REFRAC; blue) and removal of RO data assimilation (NO RO; gray) experiments. The monitoring periods were from July 10 2013 to August 10 2013 (left) and from December 10 2013 to January 10 2014 (right).

Ongoing Improvements to the NCEP Real Time Mesoscale Analysis (RTMA) and UnRestricted Mesoscale Analysis (URMA) and NCEP/EMC

Manuel Pondeca[a], Steven Levine[b], Jacob Carley[a], Ying Lin[c], Yanqiu Zhu[b], Jim Purser[a], Jeff Mcqueen[c], Jeff Whiting[a], Runhua Yang[a], Annette Gibbs[a], Dave Parrish[a], Geoff DiMego[c]

[a] *IM Systems Group Rockville, MD* [b] *Systems Research Group Colorado Springs, CO*
[c] *NOAA/NWS/NCEP/EMC College Park, MD*

NCEP's Real Time Mesoscale Analysis (RTMA) [1] system is designed to provide the highest quality gridded surface analysis for National Weather Service operations. Recent feedback from NWS forecasters has indicated that RTMA has been ineffective in resolving surface mesoscale features. In order to resolve these forecaster complaints, RTMA is being substantially changed. The use of new, higher-resolution NWP model background fields (i.e. HRRR, local NAM nests) and changes to the quality control of observations allow for a more detailed analysis that closely matches available surface observations whenever possible. New analysis variables are also being added to match those forecasted in the National Digital Forecast Database. A new analysis product (UnRestricted Mesoscale Analysis/URMA) has also been added to allow for the use of latent data in the analysis.

Background Field Improvements
Over the continental US (CONUS), RTMA's background has been a downscaled RAP 1-hour forecast [2]. The relatively coarse resolution of the RAP (13 km) with respect to the analysis grid (2.5 km) and assumptions used in the downscaling process often result in a background field that does not accurately reflect current conditions, especially over areas of complex terrain. The new RTMA's background field is a blend of a short term forecast from the new HRRR (3 km) and CONUS NAM nest (4 km) models. Downscaling effects are much less extreme when working with fields from these higher-resolution models. These models are also better able to resolve mesoscale terrain-induced features.

Quality Control Improvements
Many surface observations have previously been rejected by the RTMA due to failing the 'gross error' check that compares observations with the background field. This led to an analysis that did not match local observations, which forecasters consider inaccurate. As a remedy, two routines were added to relax the gross error check in certain situations. A terrain-aware feature relaxes the gross error check in areas of complex terrain, where the background field/model may not properly resolve the terrain. A buddy check system was also added to enable the assimilation of observations that are spatially consistent, but potentially be quite different from the background field. Obsolete, field-provided reject lists were also removed. These changes increased the number of surface observations being used in RTMA by up to 30% in some cases. Work is also beginning on a variational quality control approach, in which observations from a given station will be given a varying weight based on their differences from the current analysis solution during the minimization procedure of the variational analysis. Additional work is needed to identify and flag unrepresentative observations, which are common from some mesonet networks set up by amateur weather enthusiasts.

New Analysis Variables

Three new analysis variables have recently been added to the RTMA: total cloud cover, visibility and wind gust [3]. The total cloud cover analysis uses thinned observations of total cloud cover from the GOES 13 and 15 Imagers along with surface METAR observations of cloud cover. Wind gust and visibility analyses use available surface observations and a downscaled HRRR forecast as a background. Tests showed that blending wind gust and/or visibility background led to important mesoscale phenomena being washed out by the two models. Plans are also in place to add significant wave height (based in part on JASON-2 altimetry observations) and minimum/maximum temperature analyses. Minimum and maximum temperature analyses will only be produced once a day for the entire day.

The UnRestricted Mesoscale Analysis

The UnRestricted Mesoscale Analysis (URMA) is the RTMA run six hours later in order to incorporate observations that arrive too late for the RTMA. URMA runs currently for the CONUS domain only, but will be implemented also for the Alaska, Hawaii, Puerto Rico, and Guam NDFD domains in December 2015. URMA was recently chosen to be the "truth analysis" for the National Weather Service's National Blend of Models project.

Field Feedback

A NOAA-only internal website has been set up to allow forecasters to instantly compare RTMA/URMA analyses to previous versions of RTMA/URMA, background fields and other analyses schemes such as BDCG and LAPS. An email listserv (aor-rtma@infolist.noaa.gov) is used to keep forecasters in the field abreast of updates to RTMA and to take questions about the product, provide examples of inconsistencies or problems with the analysis.

References:

[1] Manuel S. F. V. De Pondeca, Geoffrey S. Manikin, Geoff DiMego, Stanley G. Benjamin, David F. Parrish, R. James Purser, Wan-Shu Wu, John D. Horel, David T. Myrick, Ying Lin, Robert M. Aune, Dennis Keyser, Brad Colman, Greg Mann, and Jamie Vavra, 2011: The Real-Time Mesoscale Analysis at NOAA's National Centers for Environmental Prediction: Current Status and Development. *Wea. Forecasting*, **26**, 593–612. doi: http://dx.doi.org/10.1175/WAF-D-10-05037.1

[2] Benjamin, S. G., J. M. Brown, G. Manikin, and G. Mann, 2007: The RTMA background—Hourly downscaling of RUC data to 5-km detail. Preprints, *22nd Conf. on Weather Analysis and Forecasting/18th Conf. on Numerical Weather Prediction,* Park City, UT, Amer. Meteor. Soc., 4A.6. [Available online at http://ams.confex.com/ams/pdfpapers/124825.pdf.]

[3] Zhu, Y., G. DiMego, J. Derber, M. Pondeca, G. Manikin, R. Treadon, D. Parrish, and J. Purser, 2009: Wind gust speed analysis in RTMA. Preprints, *23rd Conf. on Weather Analysis and Forecasting/19th AMS Conference on Numerical Weather Prediction,* Omaha, NE, Amer. Meteor. Soc., 15A.3. [Available online at http://ams.confex.com/ams/pdfpapers/152738.pdf.]

Data Assimilation Experiments of Radio Occultation Refractivity Data by using a Mesoscale LETKF System

[*1]Hiromu SEKO and [2]Toshitaka TSUDA
[1] Meteorological Research Institute, Japan Meteorological Agency
[2]Research Institute for Sustainable Humanosphere, Kyoto University
E-mail: hseko@mri-jma.go.jp

1. Introduction

An assimilation method of radio occultation (RO) data for a mesoscale Local Ensemble Transform Kalman Filter (LETKF) (Miyoshi and Aranami, 2006) system has been developed in this study. There are the following two difficulties in the assimilation of RO data: (1) An assumption of uniform distribution of refractivity, which is used in the estimation of refractivity profiles at tangent points, is not always valid, and (2) path-averaged data is difficult to be assimilated by LETKF system because data assimilation using LETKF is conducted by each grid point. To solve these difficulties, (1) the path-averaged refractivity was reproduced from the tangent point data and (2) path-averaged refractivity was divided into the refractivity at grid points around the path by using the ensemble average and spread obtained by LETKF system. This developed method was applied to the RO data observed on 29 July 2011. The assimilation result of this RO data indicated that the sign of the difference between the first guess and observation may be changed when the large mesoscale perturbation of refractivity exists around the tangent points, and that the temperature and water vapor are modified more widely when the path-averaged refractivity is assimilated.

2. Assimilation method of RO refractivity data

The assimilation method for a mesoscale LETKF system is composed of the following three steps: (a) a reproduction of path-averaged refractivity data, (b) a division of the path-averaged refractivity data into the grid-point refractivity around the path, and (c) data assimilation of the grid-point refractivity. Each step of the data assimilation is explained briefly in this section.

a. Estimation method of path-averaged refractivity data

The RO data at the tangent points is estimated by assuming the uniform distribution of atmosphere. Namely, RI_{tp3} is assumed to be equal to RI'_{tp3} in Fig. 1. However, this assumption is not always valid. Then, the path-averaged refractivity is produced from the tangent-point refractivity by using the following equation;

$$RI_{p1} = \frac{L_{3a}RI_{tp3} + L_{2a}RI_{tp2} + L_1 RI_{tp1} + L_{2b}RI_{tp2} + L_{3b}RI_{tp3}}{L_{3a} + L_{2a} + L_1 + L_{2b} + L_{3b}} \qquad (1)$$

where RI_{tp} and RI_p are tangent-point refractivity and path-averaged refractivity, respectively. L is the path length in each layer.

b. Division method of path-averaged refractivity into grid-point refractivity around the path

The path-averaged refractivity data was divided into the grid point values (GPVs) around the path, because it is difficult to assimilate the path-averaged data by the LETKF. The refractivity around the path is estimated by using the assumption that the modification of grid point values from the ensemble mean profile of refractivity becomes wider when the spread of refractivity and absolute values of the coefficients between the first-guess grid-point refractivity and the first-guess path-averaged refractivity are larger (Fig. 2). The grid-point refractivity is estimated by changing the ratio of the modification in order that the path-averaged refractivity obtained from the modified values becomes equal to the observed value.

c. Data assimilation by using the mesoscale LETKF system

The horizontal grid interval and domain size of the mesoscale LETKF system of this study was 15 km and 1200 x 1200 km, respectively. The ensemble size was 12. The data assimilation using LETKF started at 00 UTC 29 July 2011. The conventional observation data of the
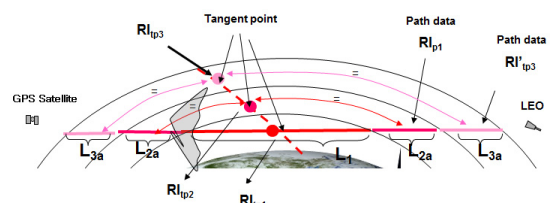

Fig. 1. Schematic illustration of the producing method of path-averaged data from the tangent-point data

Japan Meteorological Agency was used as assimilation data. The assimilation window was 6 hours and the conventional data was assimilated every hour. Three experiments were performed by changing the assimilation data. In CNTL, the conventional data was assimilated. The tangent-point refractivity data or the path-averaged refractivity data (the grid-point refractivity around the path) was added to the conventional data, and they were assimilated in TP and PA, respectively.

3. Results of data assimilation experiments

a. Vertical profiles of tangent-point and path-averaged refractivity data

In this study, FORMOSAT3/COSMIC data was used as the assimilation data. The tangent point of this RO passed east of northern Japan at 15 JST 29 July 2011 and its path extended from southeast to northwest (Fig. 3). The profiles of tangent-point and path-averaged refractivity were compared with first guess values, which were produced from water vapor and temperature of the ensemble mean.

The path-averaged and tangent-point refractivity were increased as their tangent points were lower. The difference between them became larger because the path-averaged refractivity includes small values at upper atmosphere. The observed tangent-point refractivity was larger than that of the first guess, and the observed path-averaged refractivity was larger than that of the first guess. This result shows that the sign of the difference between the first guess and observation may be changed when there were mesoscale perturbations of refractivity around the tangent points.

b. Assimilation results of refractivity data

The overall cloud distributions of TP and PA were similar to that of CNTL because the difference between them was only one data. When the tangent-point and path-averaged refractivity profiles were assimilated, a small cloud region appeared east of northern Japan and the cloud regions indicated by an arrow in Fig. 4c became smaller, respectively (Fig. 4). These changes of the cloud regions were consistent with the differences between the observed and first guess data (Fig. 3). Figure 5 shows temperature distribution at the height of 10 km. There were large mesoscale perturbations over and around Japan. This distribution supports the change of the sign of difference. The different distributions of increment of temperature from CNTL (Fig. 6) show that the wider area along the path was modified when the PA data was used. The comparisons of observed and first guess profiles between TP and PA and the wider modified regions along the path indicate that PA data should be used in the mesoscale assimilation of RO data.
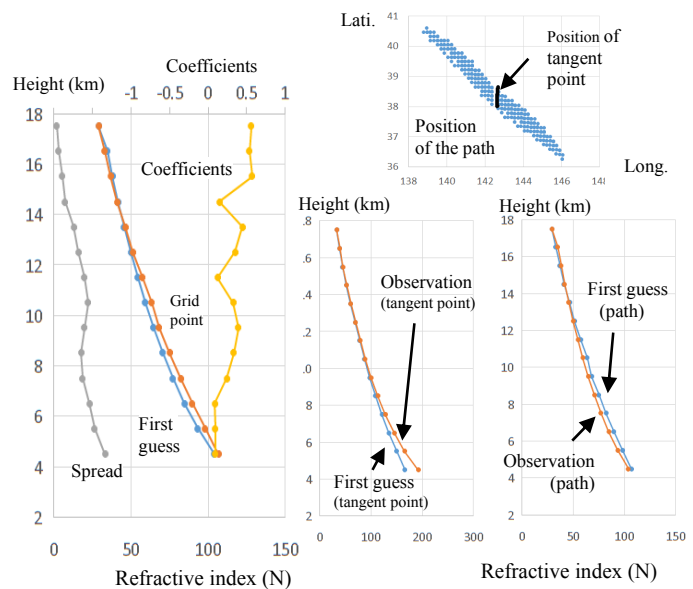
Fig. 2 Schematic illustration of producing method of grid-point refractivity from path-averaged data.

Fig. 3 Observed and first guess refractivity profiles and the positions of tangent point data and path-averaged data
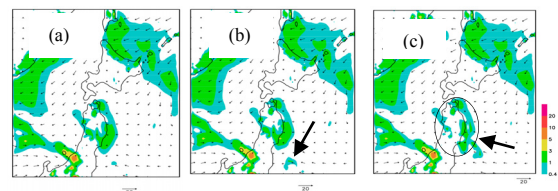
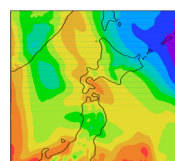Fig. 4 Cloud distributions obtained in (a) CNTL and (b) TP and (c) PA.

Fig. 5 Temperature of the first guess at the height of 10 km.
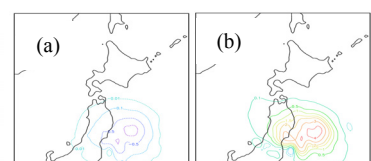
Fig. 6 Difference distributions of increment of temperature between CNTL and (a) TP and (b) PA.

References

Miyoshi, T. and K., Aranami, 2006: Application a four-dimensional local ensemble transform Kalman filer (4D-LETKF) to the JMA nonhydrostatic model (NHM), *SOLA*, **2**, 128-131.

Assimilation of rainwater estimated by the polarimetric radar for tornado outbreaks on 6 May 2012

[1]Sho YOKOTA, [1,2]Hiromu SEKO, [1]Masaru KUNII and [1]Hiroshi YAMAUCHI

[1]Meteorological Research Institute, Japan Meteorological Agency

[2]Japan Agency for Marine-Earth Science and Technology

1. Introduction

Three tornadoes were generated almost simultaneously on the Kanto Plain at about 12:30 JST (Japan standard time) on 6 May 2012. Southernmost one (hereafter, Tsukuba-tornado) was one of the strongest tornadoes in Japan (F3 in the F-scale). Northernmost one (hereafter, Moka-tornado) and middle one (hereafter, Chikusei-tornado) were estimated to be F2 and F1, respectively. It is generally not easy to simulate mesoscale vortices associated with such tornadoes because of the lack of observations required to generate realistic initial and boundary conditions for high-resolution numerical weather prediction models. In this case, however, the field associated with the tornadoes was well observed by the dense radar and surface observation network including Meteorological Research Institute Advanced C-band Solid-state Polarimetric Radar (MACS-POL). Therefore, it is expected that assimilation of these data can contribute to reproduce the mesoscale vortices more realistically. In this study, the impact to assimilate rainwater estimated by MACS-POL is discussed.

2. Assimilation experiment using the LETKF system

In this study, the nested-LETKF system (Seko et al. 2013) was used to assimilate dense observations. Figure 1 is the outline of the experiment using the one-way triple-nested system which consists of LETKF-1, 2 and 3. In LETKF-1 (horizontal grid interval: 15000 m), hourly operational observations assimilated in Japan Meteorological Agency (JMA) mesoscale analysis (radar radial wind, surface pressure and upper horizontal wind, temperature and relative humidity) were assimilated every 6 hours from 09 JST on 3 May. In LETKF-2 (horizontal grid interval: 1875 m) nested from the LETKF-1 analysis at 03 JST on 6 May, radar radial wind observed by MACS-POL and JMA operational radars in Kashiwa city and Haneda and Narita airports and surface horizontal wind, temperature and relative humidity every 10 minutes were assimilated every hour. In LETKF-3 (horizontal grid interval: 350 m) nested from the LETKF-2 analysis at 12 JST on 6 May, rainwater estimated by MACS-POL as well as observations assimilated in LETKF-2 were assimilated every 10 minutes. Finally, the downscaling forecast (horizontal grid interval: 50 m) was performed from the LETKF-3 analysis at 12:30 JST on 6 May.

Rainwater assimilated in LETKF-3 was estimated from both reflectivity Z [dBZ] and specific differential phase K_{DP} [deg km^{-1}]. Although K_{DP} is not affected by rain attenuation, a relatively large noise is found in the case of weak rain. Therefore,

$$QR \; [\mathrm{g\,m^{-3}}] = \begin{cases} QR_K & (2 \leq QR_K) \\ rQR_K + (1-r)QR_Z & (1 \leq QR_K \leq 2, \; r = QR_K - 1), \\ QR_Z & (QR_K \leq 1) \end{cases} \quad (1)$$

$$QR_Z \; [\mathrm{g\,m^{-3}}] = 10^{(Z-43.1)/17.5} \quad \text{(Sun and Crook 1997),} \quad (2)$$

$$QR_K \; [\mathrm{g\,m^{-3}}] = 3.565 \left(\frac{K_{DP}}{f}\right)^{0.77} \quad \text{(Bringi and Chensrasekar 2001),} \quad (3)$$

where $f = 5.370$ [GHz] is the frequency of MACS-POL, were used to estimate rainwater. In this study, three experiments (KR, ZR and NR) were performed with different methods of the rainwater assimilation. In KR and ZR, QR and QR_Z were assimilated as rainwater observations, respectively. In NR, rainwater was not assimilated.
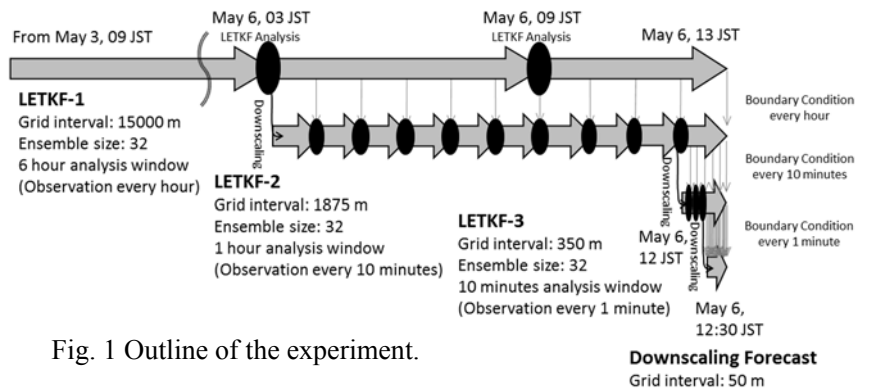

Fig. 1 Outline of the experiment.

3. Impact of the rainwater assimilation

In KR, two points of low-level maximum vertical vorticities were forecasted in south edges of hook-shaped echoes near paths of Tsukuba- and Chikusei-tornadoes at about 12:46 JST (Fig. 2), and both of them were slightly greater than those in ZR and NR. Therefore, rainwater assimilation can affect the predictability of such vortices. It seems to be caused by the modification of low-level water vapor. In fact, the region of large low-level rainwater corresponded to that of large low-level water vapor in the LETKF-3 analysis at 12:30 JST on 6 May (not shown). It means that heavy rain had large correlation with low-level water vapor at that time, and the rainwater assimilation using LETKF affected the distribution of low-level water vapor through the correlation. In this case, smaller rainwater was assimilated in ZR behind heavy rain as seen from MACS-POL than that in KR due to rain attenuation. Therefore, the more humid air was produced by the assimilation of the larger rainwater there in KR, and might affect the vorticities through the difference of the rainfall intensity.

4. Summary

Dense radar and surface observations were assimilated using LETKF in the case of tornado outbreaks, and it was succeeded to forecast two mesoscale vortices associated with tornadoes simultaneously. Rainwater assimilation affected the predictability of such vortices probably through the correction of low-level water vapor. In order to predict such vortices more accurately, clarifying relationship between the predictability and the distribution of low-level water vapor and improvement of how to assimilate rainwater are required.

References

Bringi, V. N., and V. Chandrasekar, 2001: *Polarimetric Doppler Weather Radar: Principles and Applications.* Cambridge University Press, 636 pp.

Seko H., T. Tsuyuki, K. Saito, and T. Miyoshi, 2013: Development of a Two-way Nested LETKF System for Cloud-resolving Model. *Data Assimilation for Atmospheric, Oceanic and Hydrologic Applications (Vol. II).* S.K. Park and L. Xu, Eds., Springer, 489–507.

Sun, J., and N. A. Crook, 1997: Dynamical and Microphysical Retrieval from Doppler Radar Observations Using a Cloud Model and Its Adjoint. Part I: Model Development and Simulated Data Experiments. *J. Atmos. Sci.,* **54**, 1642–1661.
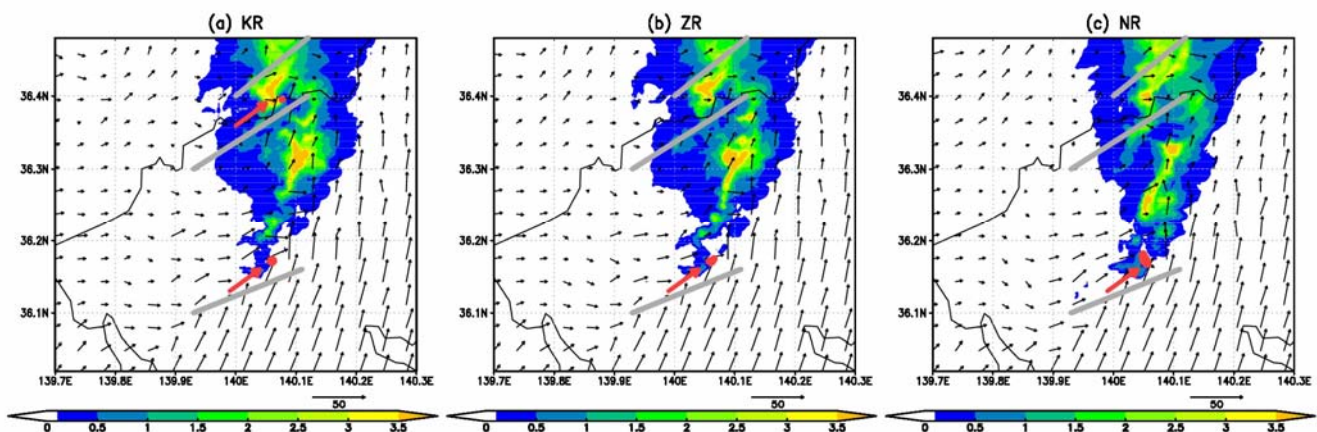
Fig. 2 Mixing ratio of rain greater than 0.1 g kg^{-1} (color, g kg^{-1}), horizontal wind (black arrows, m s^{-1}) and high-vorticity regions greater than 0.04 s^{-1} (calculated in the field coarse-grained in 350 m of the horizontal grid interval, red arrows) at 0.5 km height at 12:46 JST on 6 May in the downscaling forecast (a: KR, b: ZR, c: NR). Gray lines are observed paths of Tsukuba-, Chikusei- and Moka-tornadoes in order from south.

Status on variational correction of aircraft temperature bias at NCEP

Yanqiu Zhu[*1], John Derber[2], R. James Purser[1], Bradley A. Ballish[2], Jeffrey Whiting[1]

[1]*I.M. Systems Group, College Park, Maryland*

[2]*NOAA/NWS/NCEP/Environmental Modeling Center, College Park, Maryland*

[*]Correspondence to: 5830 University Research Ct., College Park, MD 20740; email: Yanqiu.Zhu@noaa.gov.

Aircraft data constitute one of the major sources of temperature observations, however, various studies have noted that aircraft temperature data have a generally warm bias relative to radiosonde data around 200 hPa. In this study, variational aircraft temperature bias correction is incorporated into the Gridpoint Statistical Interpolation (GSI) data assimilation system at the National Centers for Environmental Prediction (NCEP) (Zhu et al. 2015). Since each individual aircraft can have a different aircraft temperature bias, tail-number dependent bias correction is applied to the NUS-AMDAR and MDCRS data, but bias correction is applied indiscriminately without regard to tail number to all NCEP AIREP+ class data because of the lack of tail number information. A list of acronyms of instrument systems for aircraft data is provided in Table 1.
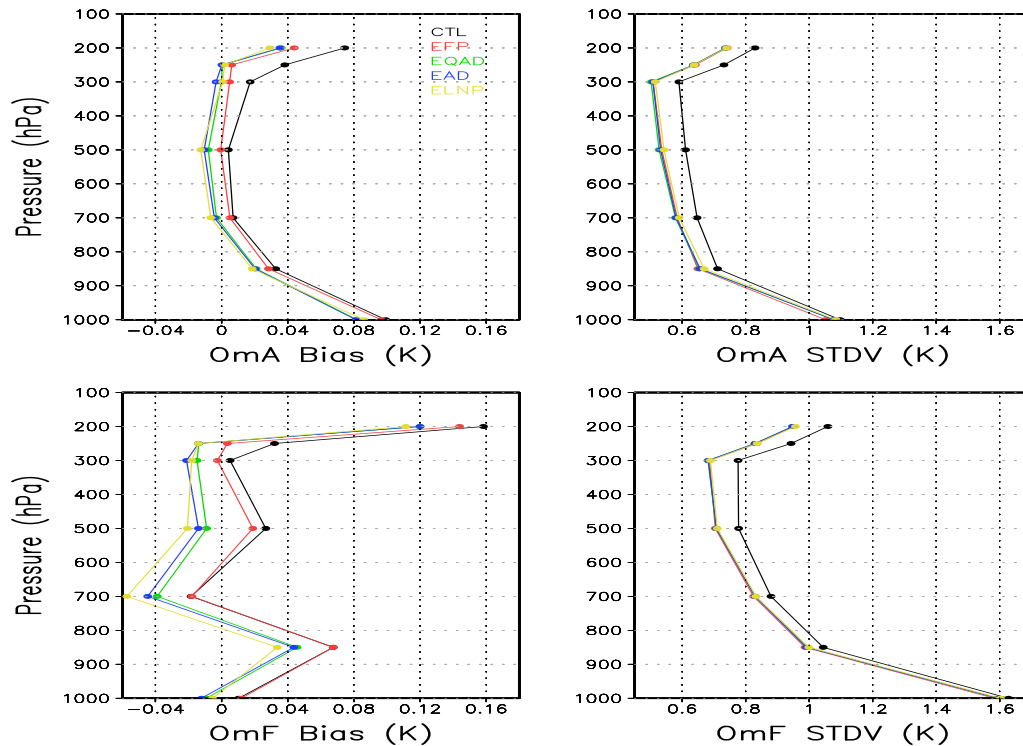

Figure 1. The biases (left panels) and standard deviations (right panels) of the OmA (upper panels) and OmF (lower panels) fits to the aircraft temperature data in experiments CTL (black line), EFP (using flight phase bias model, red line), EQAD (using quadratic aircraft ascent/descent rate bias model, green line), EAD (using aircraft ascent/descent rate bias model, blue line), and ELNP (using log-pressure bias model, yellow line) over the entire globe.

In this study, several choices of bias models are investigated in the experiments. The bias predictors use one of the following: phase of flight information; a quadratic function (i.e., three coefficients) of aircraft ascent/descent rate; separate ascending and descending linear functions of aircraft ascent/descent rate (Isaksen et al. 2012); or observation pressure information. The biases (left panels) and standard deviations (right panels) of the OmA (upper panels) and OmF (lower panels) fits to the aircraft temperature data over the entire globe are presented in Fig. 1 for the control and bias correction experiments. It is also seen that aircraft temperature bias correction cools down the atmosphere at around 200 hPa in the Northern Hemisphere, especially over the northern Atlantic Ocean and in the areas to the south-east of Australia; and improves the OmF fit to radiosonde at upper levels without degrading the fit at lower levels (Fig. 2). The improvement of the fits to GPSRO data is also observed at upper levels. Overall, the bias models using aircraft ascent/descent rate

Acronym	Description
ADS	Automatic Dependent Surveillance
AIREP	Aircraft Reports
AIREP+	Combined AIREP and coarse resolution ADS data at NCEP
AMDAR	Aircraft Meteorological Data Relay
GPSRO	Global Positioning System radio occultation
MDCRS	Automated aircraft data from U.S. aircraft
NUS-AMDAR	Automated aircraft data from outside the United States

Table 1. A list of acronyms of instrument systems for aircraft data.

outperform the others, and the quadratic ascent/descent rate bias model is slightly better than the ascent/descent rate bias model.
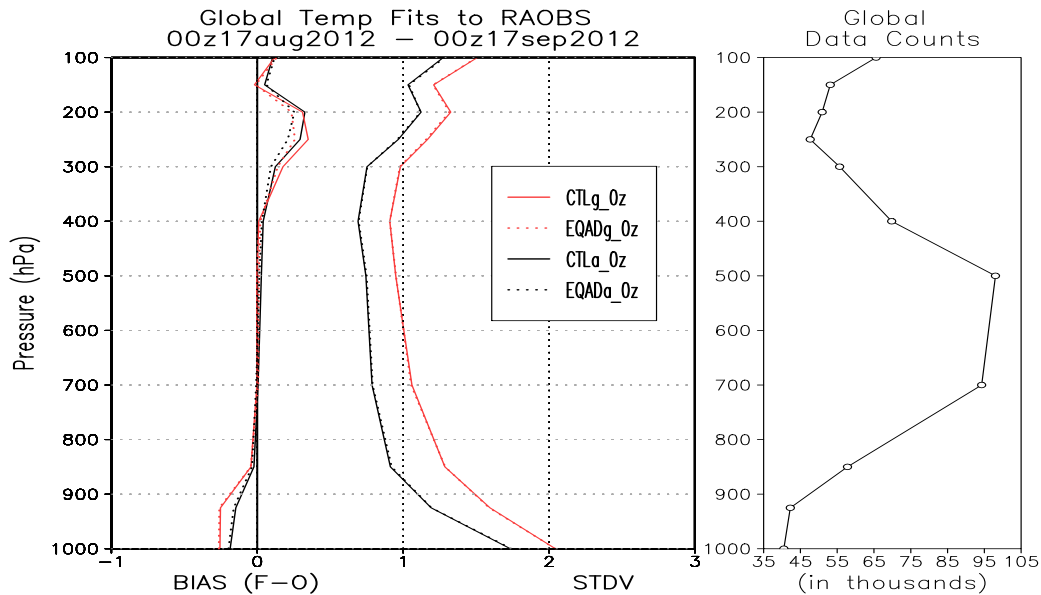

Figure 2. Bias and STDV of the fits of the first guess (red line) and the analysis (black line) to the radiosonde temperature data, i.e., First guess-minus-Observation and Analysis-minus-Observation, for experiments CTL (solid line) and EQAD (using quadratic aircraft ascent/descent rate bias model, dotted line) during the period from Aug. 17 to Sept. 17, 2012. CTLg_0Z and EQADg_0Z are the first guess fits and CTLa_0Z and EQADa_0Z are the analysis fits at 00Z.

Another issue examined in this study is the problem of too many aircraft not reporting time in seconds or too infrequently to be able to determine an accurate aircraft ascent/descent rate, which is used in the aircraft temperature bias correction as the bias predictor. In addition to the finite-difference method employed to estimate aircraft ascent/descent rate, a tensioned-splines (Tsplines) method is applied to obtain more continuously smooth aircraft ascent/descent rates and mitigate the missing time information (Purser et al. 2014). When compared to the finite difference method, it is seen that the experiment using the Tsplines ascent/descent rate as the bias predictor performs slightly better in terms of forecast fits to radiosonde data and wind forecast RMSVE in the Northern Hemisphere.

Currently the quadratic ascent/descent rate bias model with the Tsplines-based aircraft ascent/descent rate is being carefully tested in the NCEP parallel hybrid 4D Ensemble-Variational (4D_EnVar) data assimilation configuration for the next implementation. Future work includes more sophisticated bias models, which would include additional constant terms or dependence upon aircraft altitude/pressure in the quadratic ascent/descent rate bias model.

References

Isaksen, L., D. Vasiljevic, D. Dee, and S. Healy 2012. Bias correction of aircraft data implemented in November 2011. *ECMWF Newsletter*, 131, 6.

R. J. Purser, Y. Zhu, and B. A. Ballish 2014. Recovery of aircraft vertical motion profiles from incomplete data – an application of the method of splines. *NOAA/NCEP Office Note 480*, 18 pp.

Zhu, Y., J. Derber, R. J. Purser, B. A. Ballish, and J. Whiting 2015. Variational correction of aircraft temperature bias in the NCEP's GSI analysis system. *Submitted to Mon. Wea. Rev.*, under review.

Configuration of All-sky Microwave Radiance Assimilation in the NCEP's GFS Data Assimilation System

Yanqiu Zhu[*1], Emily Liu[2], Rahul Mahajan[1], Catherine Thomas[1], David Groff[1], Paul Van Delst[1], Andrew Collard[1], Daryl Kleist[3], Russ Treadon[4], John Derber[4]

[1]*I.M. Systems Group, College Park, Maryland*
[2]*Systems Research Group, College Park, Maryland*
[3]*University of Maryland, College Park, Maryland*
[4]*NOAA/NWS/NCEP/Environmental Modeling Center, College Park, Maryland*
[*]Correspondence to: 5830 University Research Ct., College Park, MD 20740; email: Yanqiu.Zhu@noaa.gov.

In the current operational NCEP's hybrid 3D Ensemble-Variational Global Forecast System (GFS), the clear-sky approach for radiance data assimilation is employed, in which radiances for cloud-free Field of Views (FOVs) and FOVs that include thin clouds are assimilated. For the FOVs that include thin clouds, the cloud signal is removed by applying a cloud liquid water bias term in the radiance bias correction scheme. The Advanced Microwave Sounding Unit-A (AMSU-A) microwave radiometer includes 12 sounding channels in the 60 GHz oxygen band, and 3 window channels at 24, 31 and 89 GHz that are sensitive to variability in water vapor, cloud and precipitation. Presently, AMSU-A channels 1-13 and 15 are assimilated in the operational GFS.

Improvements to the Community Radiative Transfer Model (CRTM) and the forecast model have been concurrent with all-sky radiance data assimilation development in the Gridpoint Statistical Interpolation (GSI) data assimilation system at NCEP. To date, cloud-affected AMSU-A radiance assimilation development has been limited to FOVs with non-precipitating clouds. These efforts have expanded the use of AMSU-A observations over cloud-affected regions. Furthermore, after accounting for non-precipitating cloud information in the inputs to the CRTM in the satellite-radiance observation operator, simulations of satellite radiances are more realistic over a much larger footprint of meteorologically active weather conditions. This has allowed us to improve the satellite radiance innovation (OmF) statistics for cloud affected FOVs, enabling the production of better analyses of temperature and moisture.

In the GFS, a cloud control variable is explicitly employed. Cloud water, including cloud liquid water and cloud ice, has been used in the clear-sky approach of the operational GFS. One of the benefits of the all-sky approach is that, the radiance data information is mapped onto not only the temperature and moisture fields, but also cloud fields via the brightness temperature Jacobians with respect to hydrometeors. CRTM does not produce a cloud Jacobian in cloud-free areas, but this is overcome by providing a very small cloud amount to the radiative transfer model in these cases. The background error covariance is composed of two parts, 75% from the flow-dependent ensemble and 25% from a static term. With the capability of choosing either individual hydrometeors or cloud water as cloud control variable(s) in the all-sky approach, a normalized cloud water control variable is used in this study to reduce spurious clouds generated from the static part of the background error covariance. While cloud analysis increments are produced through the background error cross-covariance in the clear-sky approach, additional analysis increments are generated from the projection of the radiance data information onto the cloud fields through the cloud background error variance for clouds and through the background error cross-covariance for temperature and moisture in the all-sky approach.

The symmetric observation error method (Geer and Bauer 2010; Bauer et al. 2010) is adopted in the all-sky approach for AMSU-A channels 1-5 and 15, i.e., the observation error is assigned based on the average value of cloud liquid water (Grody et al. 2001) calculated from the first guess and the observation, as the observation error for clear-sky radiance is basically the same as the one used in the clear-sky approach. On top of the symmetric observation error, additional quality control and situation-dependent observation error inflation are applied. Several factors are considered in the situation-dependent inflation: the cloud liquid water difference between the first guess and the observation, the large scattering index, the mismatched cloud information between the first guess and the observation, as well as the surface wind speed. Figure 1 displays the OmF after bias correction (left panel) for the used data and the difference in the cloud liquid water between the first guess and the observation (right panel) for AMSU-A channel 2. It is seen that the larger difference in cloud liquid water usually comes with a larger OmF.
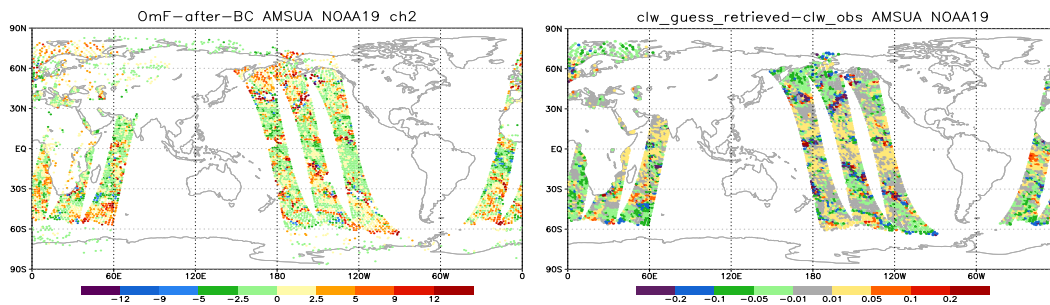
Figure 1. Used OmF after bias correction (left panel) and difference of cloud liquid water between the guess and the observation (right panel) for AMSU-A channel 2 data from NOAA19 at 00Z Oct. 27, 2013.
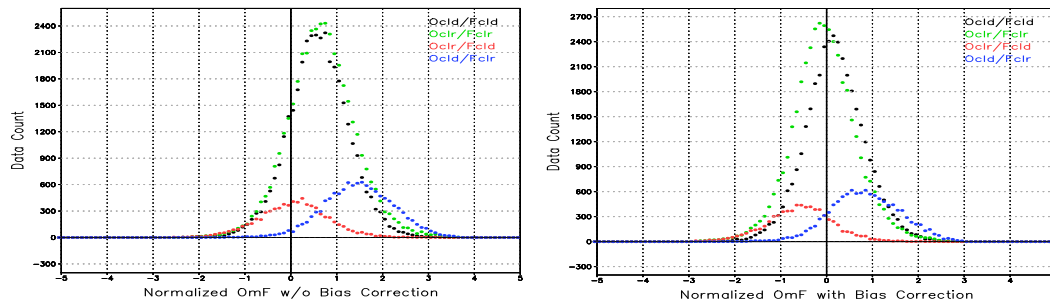

Figure 2. Histograms of OmF before (left panel) and after (right panel) bias correction for AMSU-A channel 1 data from NOAA15 for a five-days period for the four cloud catogories from first guess and observation.

As for the radiance bias correction, the cloud liquid water bias term, which is defined as the cloud liquid water difference between the guess and the observed, has been constructed in the clear-sky approach to remove the cloud signal. As this cloud liquid water bias term is no longer necessary in the all-sky approach, a new radiance bias correction strategy is formulated for the all-sky approach (Zhu et al. 2014). While all quality-controlled radiance data are used to obtain the analysis, bias correction coefficients in the all-sky approach are derived using only a selected data sample with consistent cloudy information between the first guess and the observation, and the radiance data with mismatched cloud information are bias corrected using the latest bias coefficients available. An example of histograms of OmF before (left panel) and after (right panel) bias correction for AMSU-A channel 1 data from NOAA15 is shown in Fig. 2.

The all-sky microwave radiance configuration has been tested in a T670 low-resolution hybrid 3D Ensemble-Variational GFS system. The experiment results showed a neutral impact on the forecast skill in the Northern Hemisphere but a positive impact in the Southern Hemisphere. It will soon be tested in the NCEP parallel hybrid 4D Ensemble-Variational (4D_EnVar) data assimilation system for the next implementation. Meanwhile, tests are underway on applying the averaged cloud liquid water bias term from the observation and the guess to further improve the performance of the bias correction. The balance between the analysed variables (particularly cloud, temperature and humidity) will be investigated further in the near future.

References

Bauer, P., A. J. Geer, P. Lopez, and D. Salmond, 2010: Direct 4D-Var assimilation of all-sky radiances: Part I. Implementation. *Quart. J. Roy. Meteorol. Soc.* 136, 1868.1885.

Geer, A. J. and P. Bauer, 2010: Enhanced use of all-sky microwave observations sensitive to water vapour, cloud and precipitation. Published simultaneously as ECMWF Technical Memoranda 620 and ECMWF/EUMETSAT fellowship reports 20.

Grody, N., J. Zhao, R. Ferraro, F. Weng, R. Boers, 2001: Determination of precipitatable water and cloud liquid water over oceans from the NOAA 15 advanced microwave sounding unit. *J. Geophys. Res.*, 106, 2943-2953.

Zhu, Y., J. Derber, A. Collard, D. Dee, R. Treadon, G. Gayno, J. Jung, D. Groff, Q. Liu, P.v. Delst, E. Liu, D. Kleist, 2014: Variational bias correction in the NCEP's data assimilation system. *The 19th International TOVS Study Conference (ITSC-19)*, Jeju Island, South Korea, March 25-April 1, 2014. [Available online at http://cimss.ssec.wisc.edu/itwg/itsc/itsc19/program/papers/10_02_zhu.pdf]

Implementation of Enhanced Radiance Bias Correction in the NCEP's Data Assimilation System

Yanqiu Zhu[*1], John Derber[2], Andrew Collard[1], Dick Dee[3],

Russ Treadon[2], George Gayno[1], James A Jung[4],

David Groff[1], Quanhua Liu[5], Paul Van Delst[1]

[1]*I.M. Systems Group, College Park, Maryland*

[2]*NOAA/NWS/NCEP/Environmental Modeling Center, College Park, Maryland*

[3]*European Center for Medium-Range Weather Forecasts, Reading, UK*

[4]*Cooperative Institute for Meteorological Satellite Studies, Madison, WI*

[5]*Joint Center for Satellite Data Assimilation, College Park, Maryland*

[*]Correspondence to: 5830 University Research Ct., College Park, MD 20740; email: Yanqiu.Zhu@noaa.gov.

The enhanced radiance bias correction scheme (Zhu et al. 2013)) was implemented with the latest T1534 Global Forecast System (GFS) upgrade in December 2014 at the National Centers for Environmental Prediction (NCEP). The enhanced scheme simplifies the operational suite, replacing the original two-step procedure (Derber and Wu 1998) with a single variational procedure, obtaining both the scan-dependent and air-mass dependent components along with the control variables within the Gridpoint Statistical Interpolation (GSI) data assimilation system.

One new feature in the enhanced scheme is the bias initialization step. Any new radiance data can now be used directly with the initial bias correction set to be zero. Moreover, adaptive background error variances of the radiance bias predictor coefficients are constructed. Combined with the modified pre-conditioning, which speeds up the GSI minimization convergence rate, and the new bias initialization step, the adaptive error variances offer the GSI the capability to automatically detect any new, missing or recovery of radiance data and to initialize any new radiance data. This new capability facilitates the efforts of re-analysis projects. Figure 1 displays the time series of the error variance of the global offset (red line) versus the number of radiance observations (green line) for AIRS channel 22 on AQUA. The error variance decreases rapidly to about $2.0 \times 10^{-5} K^2$ when adequate data is available, but jumps up above $6 \times 10^{-5} K^2$ twice when the observation number drops to zero, and then comes back down again when the observations recover.
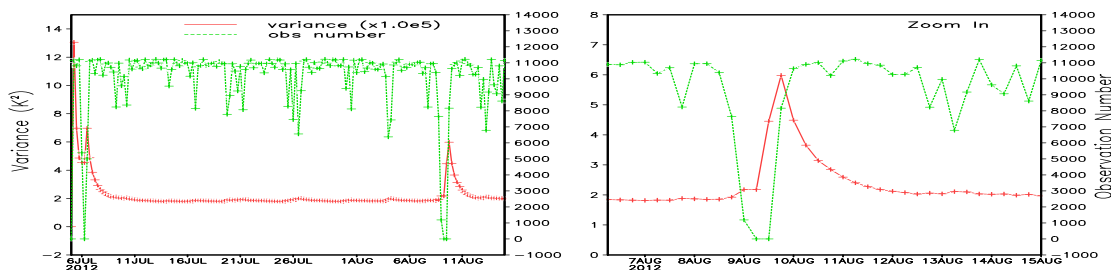

Figure 1. Time series of the background error variance of global offset (red line) and the number of radiance observations (green line) for AIRS channel 22 on AQUA (left panel). Zoomed in figure (right panel).

Another important new capability is the passive channel bias correction with a new approach formulated at the end of the analysis inside the GSI. This capability provides a very efficient way to obtain the bias estimate of any radiance data that are not used but monitored for future use, such as the data from Suomi National Polar-orbiting Partnership (NPP).

A new emissivity sensitivity predictor term has also been added to account for the land/sea difference, as the upgraded Community Radiative Transfer Model (CRTM release 2.1.3) development improves the microwave sea surface emissivity model. An example of OmF before/after bias correction for AMSUA channel 1 data from NOAA19 is given in Fig. 2 at 00Z Aug. 1, 2012. The combined effect of the two analysis components on the temperature analysis field at 700mb is presented in Fig. 3, where the upper left panel shows the analysis from **CTL** with the original radiance bias correction scheme and CRTM, the other panels are the analysis differences from the **CTL**: the lower right panel is from **CRTMonly**
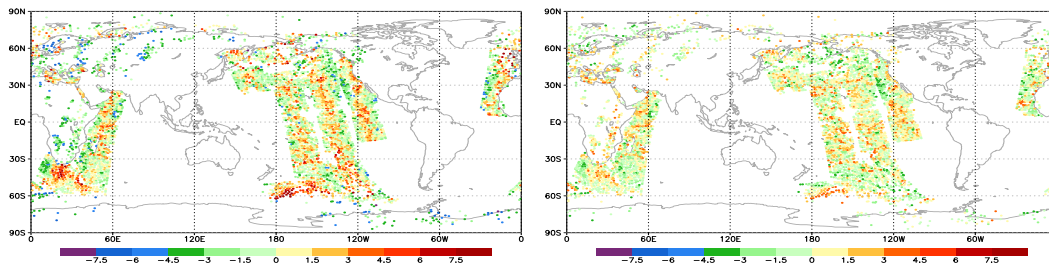
Figure 2. OmF for AMSUA channel 1 data from NOAA19 at 00Z Aug. 1, 2012: before bias correction (left), and after bias correction (right).

using the original bias correction scheme and upgraded CRTM, and the two other panels are from two slightly different configurations, **ERBCwCRTM** and **ERBCwCRTMn**, using both the enhanced radiance bias correction scheme and the upgraded CRTM. It has been known that our previous operational system has warmer temperature analyses over the southern higher latitudes at lower vertical levels when compared with the ECMWF analyses. It is seen that the use of
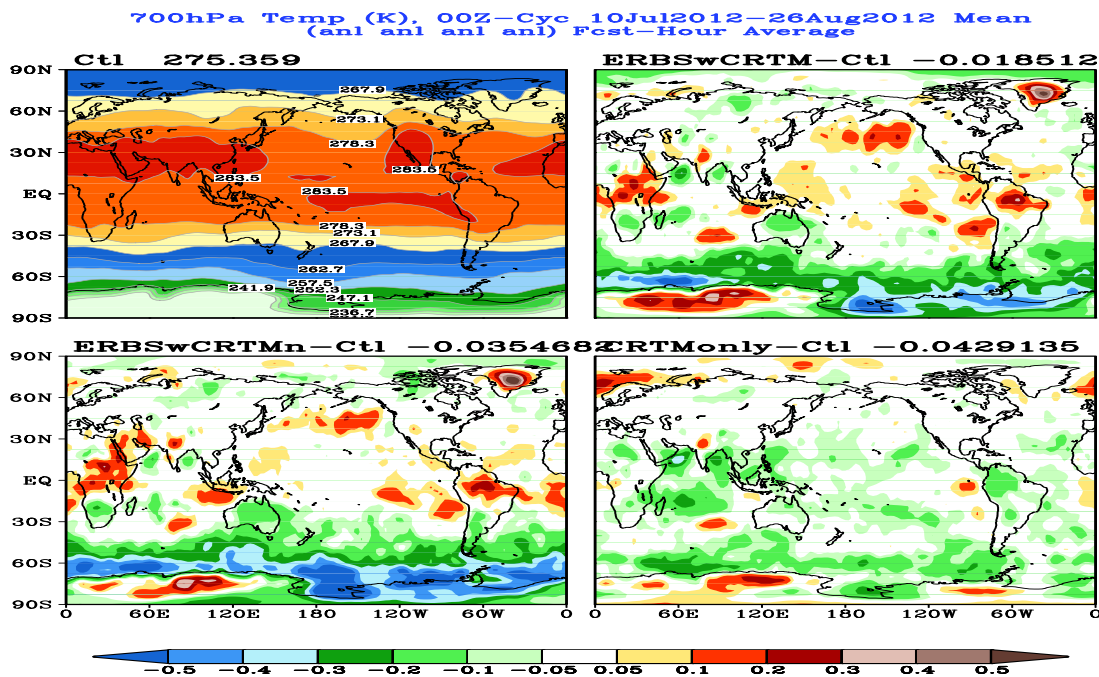

Figure 3. Mean temperature analysis field at 700mb for the **CTL** (upper left) and the analysis differences between each experiment and the **CTL** during the period from July 10 to Aug. 26, 2012: **ERBCwCRTM** (upper right), **ERBCwCRTMn** (lower left), and **CRTMonly** (lower right).

the CRTM release 2.1.3 reduces the warm bias by about $0.2K$ at southern higher latitudes, and turning on the enhanced radiance bias correction on top of the CRTM release 2.1.3 further reduces the magnitude of the warming (by as much as $0.5K$) and expands the cooling to much larger areas. The experiment results show that the enhanced radiance bias correction works well with the upgraded CRTM and provides additional significant forecast skill improvement. More details can be found in Zhu et al. 2014.

References

Derber, J. C., and W.-S. Wu 1998. The use of TOVS cloud-cleared radiances in the NCEP SSI analysis system. *Mon. Wea. Rev.*, **126**, 2287-2299.

Zhu, Y., J. Derber, A. Collard, D. Dee, R. Treadon, G. Gayno, and J. A. Jung 2013. Enhanced radiance bias correction in the National Centers for Environmental Prediction's Gridpoint Statistical Interpolation Data Assimilation System. *Q. J. R. Meteorol. Soc.*, DOI: 10.1002/qj.2233

Zhu, Y., J. Derber, A. Collard, D. Dee, R. Treadon, G. Gayno, J. Jung, D. Groff, Q. Liu, P.v. Delst, E. Liu, D. Kleist, 2014: Variational bias correction in the NCEP's data assimilation system. *The 19th International TOVS Study Conference (ITSC-19)*, Jeju Island, South Korea, March 25-April 1, 2014. [Available online at http://cimss.ssec.wisc.edu/itwg/itsc/itsc19/program/papers/10_02_zhu.pdf]